APPLICATION OF GEO-ELECTRICAL RESISTIVITY AND GRAVITY METHODS FOR GEO-HYDROLOGICAL INVESTIGATION IN MATUU; MACHAKOS COUNTY, KENYA

DOROTHY KANINI MWANZIA

MASTER OF SCIENCE

(Applied Geophysics)

JOMO KENYATTA UNIVERSITY OF

AGRICULTURE AND TECHNOLOGY

2019

Application of Geo-Electrical Resistivity and Gravity Methods for Geo-Hydrological Investigation in Matuu: Machakos County, Kenya

Dorothy Kanini Mwanzia

A thesis submitted in partial fulfillment for the Degree of Master of Science in Applied Geophysics in the Jomo Kenyatta University of Agriculture and Technology

2019

DECLARATION

This thesis is my original work and has not been presented for a degree in any other university.

Signature ……..... Date …….

Dorothy Kanini Mwanzia

This thesis has been submitted with our approval as University supervisors:

Signature ……..Date …….

Dr. K'Orowe Maurice, PhD
JKUAT, Kenya

Signature ……..Date …….

Dr. Githiri Gitonga, PhD
JKUAT, Kenya

DEDICATION

I dedicate my entire work to God Almighty, my Father, Mwanzia Munuve, and my dear Mother, Mary Mwanzia, who have always encouraged me to pursue my dreams.

ACKNOWLEDGEMENT

First, I wish to acknowledge and thank the heavenly Father for providing all the resources I needed to do this project.

Secondly, I deeply wish to appreciate my supervisors: Dr. K'Orowe and Dr. Githiri of Jomo Kenyatta University of Agriculture and Technology (JKUAT).They have treated me as a daughter, provided wise counsel, been patient and always found time to read my work. I would also like to extend my gratitude to my loving dad, mother and siblings for offering a shoulder to lean on when it got tough.

Thirdly, I would like to thank the Society of Exploration Geophysicists (SEG) Field Camp Foundation Program, for financing this project. I am also grateful to the Jomo Kenyatta University Geophysical Society members for helping me collect data in the field. The JKUAT administration has been instrumental in facilitating my studies and providing some of the geophysical equipments that I used in the field.

Finally, I would like to thank my friends Evance Odero, Leah Mwangi and Kelvin Lodenyi for providing me with words of affirmation and encouragement during my research period.

TABLE OF CONTENT

LIST OF TABLES

LIST OF FIGURES

LIST OF APPENDICES

LIST OF ABBREVIATIONS AND ACRONYMS

DC	Direct current
STN	Station
EMBS	Eastern Mozambique Belt Segment
GPS	Global positioning System
IGSN	International Gravity Standardization Network
SSR-MP-ATS	Signal Stacking Resistivity Meter
ER	Electrical resistivity
CG5 Model	Scintrex Autograv System
POI	Point of Inflection
GF	Universal Gravitational field
FAC	Free Air Correction
LC	Latitude Correction
EMBS	Eastern Mozambique Belt Segment
VES	Vertical Electrical Sounding
G	Gravitational constant
ZOI	Zone of interest
R_w	Water resistivity
R_t	Formation resistivity
$\rho_{a\alpha}$	alpha resistivity measurement
$\rho_{a\beta}$	beta resistivity measurement
$\rho_{a\gamma}$	gamma resistivity measurement
ρ_m	mean geometric resistivity
ρ_{at}	Apparent resistivity measured perpendicular to strike
ρ_{a1}	Apparent resistivity parallel to fracture strike

LIST OF SYMBOLS

ρ	Resistivity
ρ_a	Apparent resistivity
Ω	Ohm
e	Exponent
π	Pi
θ	Fracture Strike Azimuth
ϕ	Porosity
A	Anisotropy
F	Force
r	Separation distance
Δ	Delta
N	Bedrock Anisotropy
λ	Apparent anisotropy
V	Voltage
I	Current
K	Geometric Constant
"a"	Square Length
'a'	Latitude
D	Drift
H	Height

ABSTRACT

In Kilango-Matuu area, ground water potential zones cover a small area because the region receives low amounts of rainfall of about 800 millimeters (Approximately) annually. Hard rocks dominate the area that result to small region ground water potential zones. In regions with such characteristics, chances of ending up with a dry well are high when drilling for ground water before carrying out correct and accurate preliminary processes. In this research, the main aim was to delineate ground water potential zones within Kilango Matuu–Machakos. In order to achieve this, a proper understanding of the subsurface formation and faults/fractures, which are the main ground water conduits, was inevitable. Therefore, Geo-electrical technique and gravity methods were deployed over a 25 square kilometer area. Subsurface water bodies conductivity measurements were taken as well to help in determining the porosity of the region. Azimuthal square array was deployed and data obtained was utilized in generating a graph of the apparent anisotropy versus the bedrock anisotropy, which displayed a slight change in bedrock anisotropy against a significant change in apparent anisotropy. This array required just 35% of the surface area used for an equivalent survey using other geo-electrical resistivity arrays. These two advantages justified the choice of this array over the most commonly utilized Wenner and Schrumberger arrays. Graphical and analytical analysis displayed presence of a fracture within the porous zone oriented along NE-SW direction. The crossed square array data detected a fracture strike along 039^0 azimuth. In summary, Kilango-Matuu region has a possibility of having several fractures with the main one being oriented along 049.56622^0 orientation. The geometric resistivity values of interest were qualitatively analyzed and a low resistive and a less porous zone was detected in the western part of the study area. Computed porosity had values ranging from 0.1648 to 0.2922. In gravity survey, 156 stations were established and corrections were carried out on the observed gravity values. A bouguer anomaly contour map was generated which indicated presence of a subsurface formation with low density along the western side of the study area. A cross-section AA' was cut across the zone of interest and imported to Euler software and Euler deconvolution was done, which indicated a discontinuity covering about 600 meters distance. In order to understand the stratigraphy of the study area, the data obtained from the cross-section AA' was uploaded on Grav2dc and a 2D forward model was attempted. Results from this study indicate that, Matuu-Kilango area has a fractured basement rock, which is capable of holding and transmitting ground water.

CHAPTER ONE

INTRODUCTION

1.1 Background study

In dry areas, most people rely on ground water for domestic and agricultural purposes. Movement and properties of ground water are determined by the nature of the basement rock that surrounds the aquifer (Batte, Muwanga, Sigrist, & Owor, 2008). In hard rock environment, fractures and faults are the main structures that provide for potential groundwater transmission and storage. In most cases, these structures are highly localized and therefore, hard to locate.

To delineate fractures/faults, techniques such as geo-electrical resistivity and gravity methods are applied (Sri & Oliver, 2003). These two methods are widely accepted means of ground water exploration. The other techniques, which are also applicable in ground water exploration include, magnetic and seismic methods. Application of geophysical techniques has improved the efficiency and cost effectiveness in geophysical field surveys. Research that has been conducted so far shows that, groundwater resources in eastern part of Kenya are underdeveloped (Ndeto, 2011). Parts of Machakos County, Kenya which receives low amounts of rainfall of about 800mm annually, several organizations including the world vision have invested in exploring for ground water resources in the area (Omoyo,Wakhungu, & Oteng'i, 2015). However, in most cases researchers from these organizations conduct survey using only VES array and end up drilling dry wells (Ndeto, 2011). Therefore, there is need for detailed geophysical survey that involves proper understanding of the area geology to improve on the efficiency and accuracy of the information used when drilling wells.

1.1.2 Study Area

The study area is Matuu-Kilango area in Machakos County. The area lies along the Eastern Mozambique Belt segment. The study area is bounded by Latitudes 1^{o} 05'S and 1^{o}08'S and Longitudes 37^{o} 31'E and 37^{o} 33'E zone 37M and its digital elevation is illustrated in the Figure 1.1.

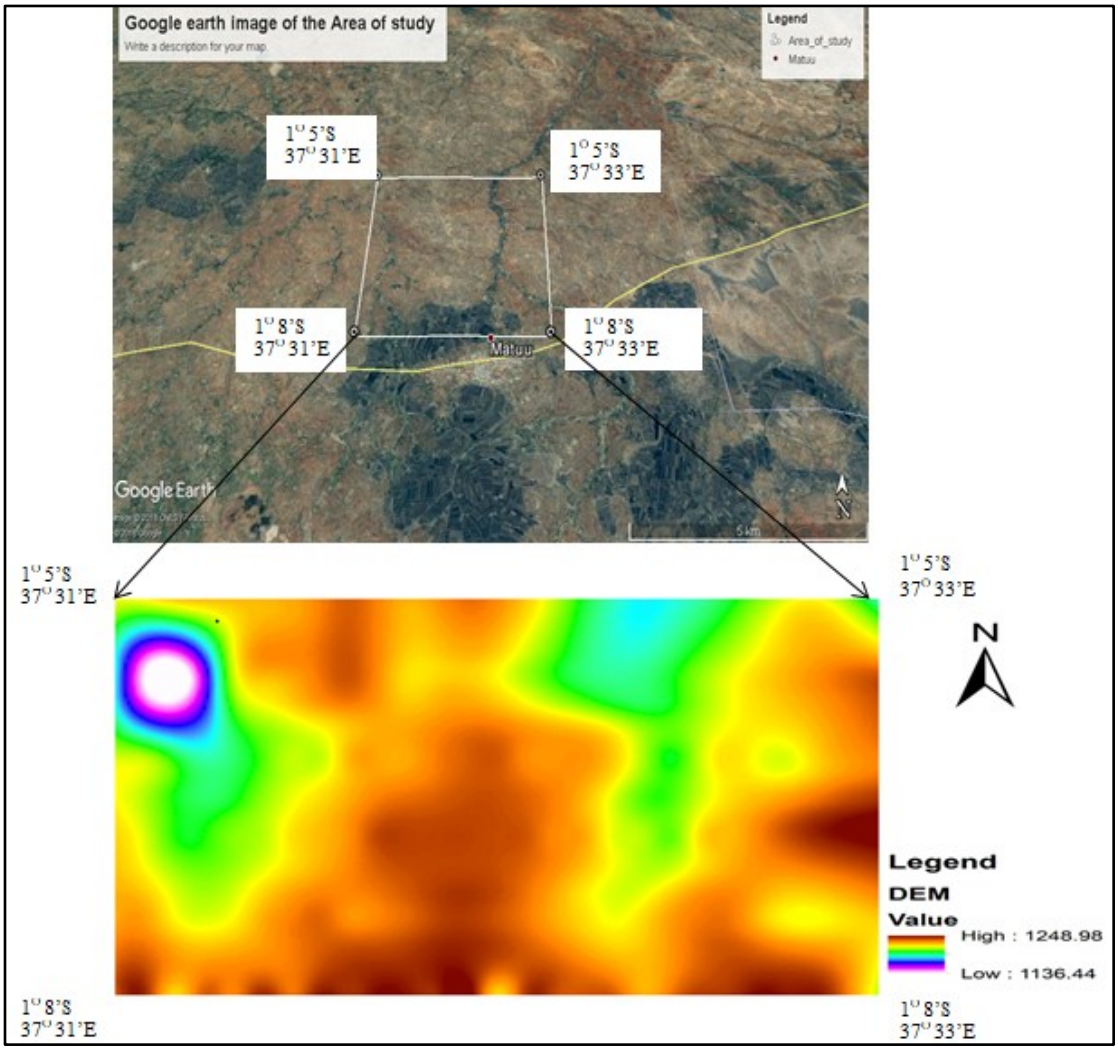

Figure 1.1: Location of the study area (Survey of Kenya, 2005)

1.1.3 Geology of the Study Area

The study area is located in the Eastern side of Gregory Rift valley. Prior to the formation of the Rift valley, the entire Matuu area was characterized by Precambrian basement crystalline rock system of Mozambique belt segment (EMBS) which stretches in Kenya for about 800 km length and 200 km width at 3^0 N and 4^0S latitudes and between 37^0E and 39^0E longitudes (Mathu, 1992). These rocks have gone through a cycle of metamorphism, exposure and erosion. The surface rocks comprises of metamorphic rocks overlain by a Yatta Plateau to the south. The formation of Yatta plateau begun at the start of Miocene period by eruption of Phonolites (Mathu, 1992). This resulted into a large part of sub-Miocene surface being covered by lava. This geological system holds water in a network of fractures and faults since the metamorphic rocks are non-porous and impervious. The study area is described by meta-intrusive mafic and ultramafic rocks that include Diorites, Gabbros, Anorthosites, Peridotites and Picrites. The mafic and ultra-mafic rocks occur in the general Machakos area and its environment (Nyamai Mathu, Opiyo, & Wallbrecher, 2003). The study area (Matuu-Kilango) is largely semi-arid.

1.1.4 Detailed geology of the Study Area

The Basement system in the project area is undifferentiated (Figure 1.2). It is believed to represent an original sedimentary series of limestones, shales and sandstones, into which basic magma has been intruded. Intense compression with rising temperature has resulted in these rocks being transformed into highly folded metamorphic series. The metamorphic rocks vary in grain size from fine-grained schists to coarse gneisses and in composition from pure quartzites and marbles to plagioclase amphibolites (Bear, 1952).

What Crowther (1957) terms the ‘basement system’ in the Matuu-Kilango area as Archaean rocks largely composed of banded semi-pelitic and politic mica-amphibole-quartz-Feldspar schists and gneisses with inter-banded psammitic type rocks, and intense

granitic sheet (and vein) intrusion and migmatization. These basement rocks are also intruded by coarse Archaean porphyritic granites. The overlying recent black soils in this area are evident towards the south and south east.

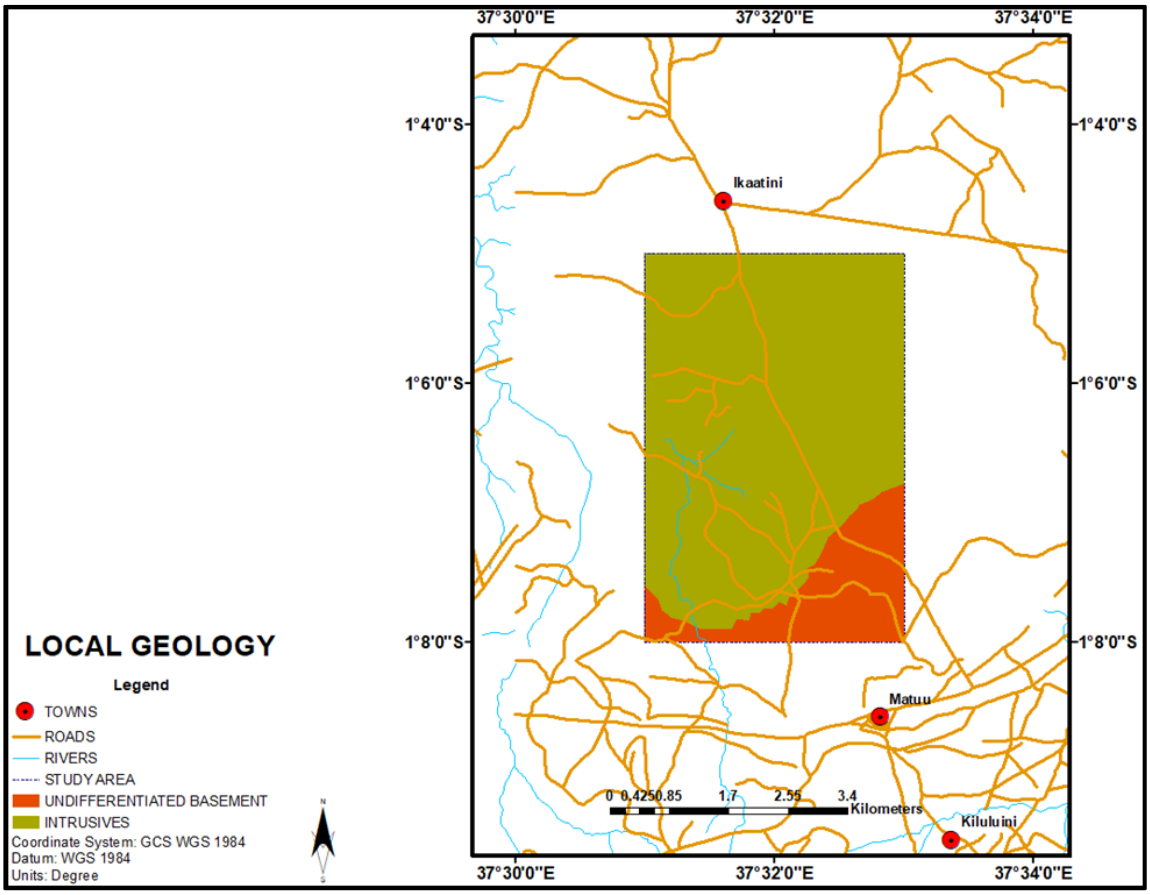

Figure 1.1: Geological map of the study area (Nyamai *et al.,* 2003)

1.2 Problem Statement

Surface water is scarce in Eastern part of Kenya and so it is important for research to be conducted with an aim of getting a substitute for the source of this great resource. The study area is underlain by hard bedrock. Therefore, locating siting ground water potential zones is a challenge. Previously, researchers have used vertical electrical sounding technique to site boreholes in the area. In most cases, people who have relied

on the information obtained from this single technique have ended up drilling dry wells. This investigation tries to solve the problem of improper delineation of fracture strikes/faults, which are the major ground water conduits hence, the aquiferous units.

1.3 Justification

The geology of Kilango-Matuu area shows presence of hard rocks that underlie the region. In regions dominated by hard rocks, an aquifer formation originates from secondary porosity through fractures/faults. Vertical Electrical Sounding (VES) frequently used in locating fractures and faults is less sensitive to the rock anisotropy compared to the methods deployed in this research. Azimuthal resistivity method is an improvement of resistivity method where the magnitude and direction of the electrical anisotropy are determined. It is generally believed that anisotropy is caused by the presence of fluid-filled fractures in relatively resistive rock or soil.

1.4 Objectives

1.4.1 General Objective

To delineate ground water potential zones within the basement rock region of Kilango-Matuu, Machakos County using azimuthal square array and gravity techniques.

1.4.2 Specific objectives

1. To determine the orientation of the main fractures using resistivity method
2. To determine the subsurface density variation using gravity technique
3. To delineate possible aquifers in the region and their inferred geometry using resistivity and gravity technique
4. To develop a geo-hydrological model for the area

CHAPTER TWO

LITERATURE REVIEW

2.1 Geophysical Methods

Traditional methods like trace analysis and the trial and error borehole drilling methods have been used for groundwater exploration for decades. These methods are applied based on the hypothesis that correlation exists between fracture traces and the occurrence of groundwater. Separating natural features from man-made features is a very common challenge for inexperienced geologists in the field. Features such as roads, railroads and fences are often confused with naturally occurring fracture traces on topographic maps because they tend to exhibit similar linear geometric patterns (Lattman, 1958). This study demonstrates the importance of accurate interpretation of fracture traces and the benefit of field proofing in establishing reliable data in groundwater exploration using geophysical techniques. For instance, in areas with Banded Gneissic Complex, aquifers present have high yields of the available ground water compared to areas with basalt rocks (Sivaramakrishnan, Asokan, Sooryanarayana, Hegde, & Benjamin, 2015). In different places, aquifers have different degree of ground water occurrence depending on the type of rocks in the area (Archie, 1942).

2.1.1 Geo-Electrical techniques

Geo-electrical techniques are useful for discovering unknown subsurface conditions. Geo- electrical methods are used in collecting the subsurface information related to the electrical properties of the earth material. This method measures variations in material's physical properties. For groundwater investigations, the most significant parameters used in describing an aquifer system are the ones that are related to the porosity and permeability of an aquifer as well as the surrounding aquitard (Sri & Oliver, 2003). Use of geo-electrical techniques increases cost effectiveness by reducing the number of boreholes needed to "hit" a geological target.

Electrical conductivity/resistivity is a proportionality factor relating the electrical current that flows in a medium to the applied electric field. It has been correlated with porosity (Archie, 1942). K'Orowe, Nyadawa, Singh and Rangarajan, (2012) utilized resistivity method on a typically hard rock terrain found in the Jangaon sub-watershed, Andhra Pradesh, India. The study showed linear relationship between transmissivity and formation factor. A related study carried out by Muturi, K'Orowe, Githiri, Cezar and Jeffrey, (2013) in Kitui on evaluation of ground water potential, employed electrical resistivity that inferred existence of shallow aquifers in the area. This conclusion was made after the geo-electrical data collected displayed low resistive zones between high resistive zones at reasonable depths. Odero, K'Orowe and Githiri (2016) carried resistivity survey in Kilango-Matuu area involving Wenner and Schlumberger array techniques. Anomalous low resistive zone was observed, which after computational analysis, showed the inferred aquifer.

Antony, (2012), carried out electrical resistivity (DC) survey to delineate water-bearing zones within the Qaurtzite Terrain at Edaikkal, Ambasamudram, tirunelveli. In the study, he deployed the Azimuthal Square Array Configuration and was able to identify the aquifer thickness within the study area. He also conducted a ground water prospecting survey in Sanganoor, Coimbatore District, Tamilnadu, India where he deployed the same array and managed to estimate the ground water yield within the area. The azimuthal square array configuration can be applied in the study of the discontinuities in the subsurface as result of fractures/faults within the basement rock (Habberjam and Watkins, 1967).

Reynolds, (1998) used vertical electrical sounding technique in carrying out a survey for a rural water supply in northern Nigeria. Several other scientists have demonstrated the use of the geo-electrical resistivity survey for groundwater exploration in crystalline basement aquifers in sub Saharan Africa. These include, (Batte *et al.,* 2008), (Foster, Chilton, Moench, Cardy, & Schiffler, 2000) and (Singhal & Gupta, 2010). The

challenges associated with the methodology employed in these studies related to result interpretations that required site knowledge and critical thinking skills.

Most of geo-electrical techniques use various electrode arrays that can be deployed in ground water exploration. These includes the Azimuthal square array, Wenner, Schlumberger, pole-pole, pole-dipole, dipole-dipole, general incline array, gradient array and the gammar array **(**Lashkaripour, 2003). The azimuthal square array has two unique advantages over the other configurations. The azimuthal square array is more sensitive to the bedrock anisotropy in the subsurface and requires less surface area compared to the other arrays (Lane, Haeni and Watson, 1995). A rock is said to be electrically anisotropic if the value of vector measurement of its resistivity varies with direction (Taylor and Fleming, 1988; Watson and Barker, 1999). These two advantages made it the most suitable array for use in this study. Matias and Habberjam (1986), Watson and Barker (1999) and Busby (2000) have shown that when using azimuthal resistivity survey, any observed change in apparent resistivity (ρ_a) is interpreted as an indication of fracture anisotropy, which in most cases might also be produced by the presence of a dipping bed or in homogeneities or lateral changes in apparent resistivity. When carrying out a geophysical method is it very important to deploy two or more methods to improve on the accuracy of the findings. The other method suggested in this research is Gravity method.

2.1.2 Gravity methods

This method is commonly used in mapping areas of low-density within a more dense rock. It can also be applied in detecting voids within the subsurface. Bisson and Lehr, (2007) used gravity method in groundwater exploration and in the detection of structural trends controlling the regional geometry of the groundwater aquifers. Gravity survey was conducted in crystalline rocks in India during groundwater exploration and the results showed that, areas of more deeply weathered granite that contained wells of

higher groundwater yield were represented by negative gravity values (Murty & Raghavan, 2002).

Micro-gravity surveys are mainly conducted to record the changes in density of materials. Rock fracturing and weathering increases porosity, thereby reducing its bulk density (Mishra, 2011). Gravity anomalies due to weathering of the rocks in the subsurface are so significant to an extent that they can be detected. Overmeeren (1975) used micro-gravity approach for groundwater evaluation near Taltal province of Antofagasta. Mark, (1980) was able to delineate major features of the bedrock surface from a gravity survey of a buried deep valley in Wisconsin, U.S.A.

Investigation for groundwater potential resources in rock county Minnesota showed that gravity method is an effective reconnaissance-scale tool for ground-water exploration (Chandler, 1994). Groundwater exploration utilizing gravity method as one of the geophysical method was successfully conducted at the central part of Sinai Peninsula, Egypt (Sultan, Mekhemer, Santos, & Alla, 2009). Gravity method is used in determining the gravity anomalies due to differences in local masses and their depths. Any increase in gravitational pull on a mass at the end of weight arm is caused by a rotation opposed through a sensitive spring. This is achieved by modeling the corrected complete bouguer anomaly data and making assumptions on density contrast of rock units (Yutsis,Yaneth, Konstantin, Juan & Gabriel ,2012). According to Goldman, Rabinovich, Gilad, Gev and Schirov, (1994), Electrical Resistivity (ER) and gravitational field (GF) have a close relationship. The relationship is displayed by the electrical conductivity and the physical properties of an aquifer that include the conductance and the resistance, thus ER and GF are the most commonly used methods in hydrogeological applications. Several softwares are used in analyzing geophysical data. In this research surfer 10, 2D Euler deconvolution and Grav2dc softwares were utilized.

2.2 Software description

2.2.1 Surfer 10 software

Surfer is a powerful contouring, gridding and surface-mapping program. Surfer has numerous analysis tools useful in discovering depths of gravity and geo-electric data. Surfer enables adjustment of interpolation and gridding parameters, assess the spatial continuity of data with variograms, define faults and break lines. Surfer's outstanding gridding and contouring capabilities have made it the software of choice for working with XYZ data (Trochu, 1993).

Its capability of customizing the map display and annotating with text creates attractive and informative maps. Kriging weights the surrounding measured values of ground resistivity and gravity to derive a prediction for an unmeasured location. The general formula for both interpolators is formed as a weighted sum of the data:

$$\hat{Z}(S_O) = \sum_{i=1}^{N} \lambda_i Z(S_i) \quad \text{.....2.1}$$

where: $Z(s_i)$ is the measured value at the ith location, λ_i is an unknown weight for the measured value at the ith location, s_0 is the prediction location, N is the number of measured values.

2.2.2 2D Euler Deconvolution Software

This software is used in constraining the subsurface and plotting cross-sections imaging the subsurface structures along profile lines. 2D Euler deconvolution software is a two-dimensional computer program used to image subsurface depth gravity sources using potential field derivatives (Cooper, 2006). This software's popularity is largely due to its great simplicity of implementation and use, making it the tool of choice for a quick initial interpretation (Mushayandebvu, Lesur, Reid and Fairhead, 2004). Conventional

2D Euler deconvolution software uses three orthogonal gradients of any potential quantity as well as the potential quantity itself as shown in equation 2.2 to determine the depths and locations (body geometry) of a source body within the subsurface.

$$(x-x_0)T_{zx}+(y-y_0)T_{zy}+(z-z_0)T_{zz}=N(B_z-T_z)\quad\ldots\ldots\ldots\ldots\ldots\ldots\ldots\ldots\ldots\ldots 2.2$$

This equation is for complete bouguer anomaly vertical component T_z of a body having a homogeneous gravity field. x_0, y_0 and z_0 are the unknown co-ordinates of the source body centre or edge to be estimated and x, y and z are the known co-ordinates of the observation point of the gravity and the gradients. T_{zx}, T_{zy} and T_{zz} are the measured gravity gradients along the x, y and z directions. N is the structural index and B_z is the regional value of the gravity to be estimated.

2.2.3 Grav2dc Software

Grav2dc software performs calculations of gravitational anomaly over one or more 2D bodies. Grav2dc for Windows allows forward modeling and inversion of gravity data. The bodies making up the model have their predicted densities displayed on them. This modeling software calculates gravitational attraction at each observation point due to polygonal shaped bodies, with each body having a specific density (Cooper, 2004).

2.3 Theoretical Concepts

2.3.1 Resistivity Method

Ohm's law provides fundamental equation for resistivity survey. In Figure 2.1, ρ is resistivity, R is resistance, L is length of homogenous conducting cylinder and A is cross-sectional area.

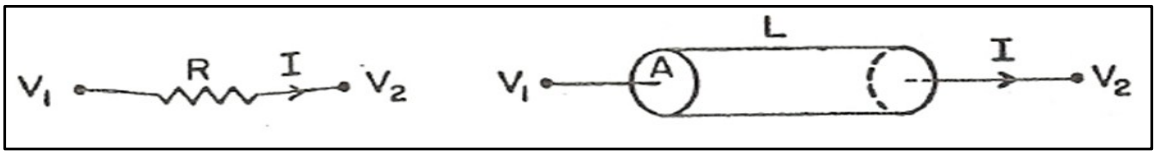

Figure 2.1: Electrical conducting elements of the earth material (Smith and Alley, 1992)

R of a cylindrical material is directly proportional to the length of the cylinder, L, and inversely proportional to the cross sectional area, A.

$$R = \frac{\rho L}{A} \quad \text{..... 2.3}$$

where ρ is the electrical resistivity of the cylindrical material.

The intrinsic property of the earth material, electrical resistivity, (ρ), can be defined from the formula:

$$\rho = \frac{RA}{L} \quad \text{.....2.4}$$

where R (Ω) is the resistance of the element and is directly proportional to its length, L (m) and inversely proportional to the cross-sectional area A (m^2).

From Ohm's law

$$I = \frac{V}{R} = \frac{1}{\rho} A \frac{\Delta V}{L} \quad \text{..... 2.5}$$

From which;

$$V = \frac{I\rho}{4\pi r} \quad \text{..... 2.6}$$

For homogeneous half space, the potential at any point due to a current source at the surface of a homogeneous earth is given as;

$$V = \frac{I\rho}{2\pi r} \quad \text{……...……...…2.7}$$

where ρ is the resistivity of the ground and I is the current injected into the ground.

For solid earth, which is anisotropic and not like a straight wire, equation 2.7 is customized to;

$$\rho = \frac{\Delta V}{I} 2\pi r \quad \text{…….……...……...……...…2.8}$$

whereby ΔV is change in voltage.

Since the solid Earth is not homogeneous then equation 2.8 is re-written as;

$$\rho_a = \frac{\Delta V}{I} 2\pi r \quad \text{……...……2.9}$$

Equation 2.9 denotes the resistivity of the earth if it were homogeneous.

The $2\pi r$ in equation 2.9 is defined as the geometric factor (K). This factor is usually configuration dependent. This study utilized the Azimuthal square array configuration.

2.3.1.1 Azimuthal square array configuration

The azimuthal square array configuration has its electrodes placed at corners of a square with sides of length ("a") in meters (Figure 2.2).

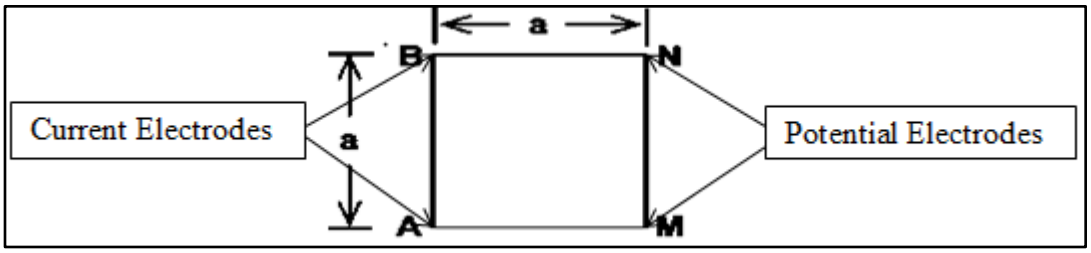

Figure 2.2: Azimuthal square array (Keary, Brooks and Hill, 2002)

A measurement point location was assigned at the center of the square and three resistivity measurements were taken; two in perpendicular direction and one in diagonal direction. These measurements were taken with respect to the square geometry denoted as alpha, beta and gamma (Figure 2.3). The depth of investigation is approximately equal to length ("a") but this is resistivity dependent. Azimuthal square array electrical resistivity configuration is effective in characterizing fracture orientation in shallow bedrock environment (Bills, Truini, Flynn, Pierce, Catchings & Rymer, 2000).

Substituting geometric constant K in equation 2.9 we obtain,

$$\rho_a = \frac{K\Delta V}{I} \quad \text{.....2.10}$$

ρ_a is the apparent resistivity, K is the geometric factor, I is the injected current and ΔV is the potential difference. Equation 2.10 is used in determining apparent resistivity from Azimuthal Square array (Habberjam & Watkins, 1967).

To take care of directions of array and geometry correlations the mean geometric apparent resistivity from the azimuthal square array measurements was calculated using equation 2.11 (Lane *et al.,* 1995).

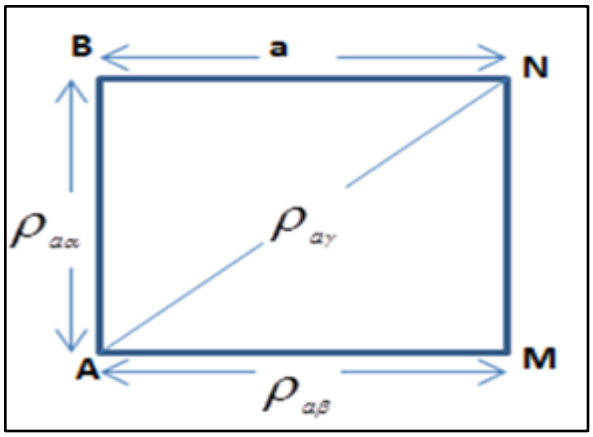

Figure 2.3: Azimuthal Square array deployment (Bills et al., 2000)

$$\rho_m = \sqrt{(\rho_{a\alpha})(\rho_{a\beta})} \quad \text{.....2.11}$$

where $\rho_{a\alpha}$ is alpha resistivity, $\rho_{a\beta}$ is beta resistivity and ρ_m is mean geometric resistivity.

2.3.1.2 Crossed square array

Crossed square array data deduced from azimuthal square array data was analyzed to give fracture strike azimuth (Habberjam, 1975).

$$\theta = \frac{1}{2} TAN^{-1}\left[\frac{\left(D^{-2} - C^{-2}\right)}{\left(A^{-2} - B^{-2}\right)}\right] \quad \text{……..……2.12}$$

where θ is the fracture strike azimuth and;

$$A = \left[\frac{(\rho_{a3} + 3\rho_{a1})}{2} + \frac{(\rho_{a4} + \rho_{a2})}{(2)^{\frac{1}{2}}}\right]\left[\left(2 + (2)^{\frac{1}{2}}\right)\right] \quad \text{2.12a}$$

$$B = \left[\frac{(\rho_{a1} + 3\rho_{a3})}{2} + \frac{(\rho_{a2} + \rho_{a4})}{(2)^{\frac{1}{2}}}\right]\left[\left(2 + (2)^{\frac{1}{2}}\right)\right] \quad \text{2.12b}$$

$$C = \left[\frac{(\rho_{a4} + 3\rho_{a2})}{2} + \frac{(\rho_{a1} + \rho_{a3})}{(2)^{\frac{1}{2}}}\right]\left[\left(2 + (2)^{\frac{1}{2}}\right)\right] \quad \text{2.12c}$$

$$D = \left[\frac{(\rho_{a2} + 3\rho_{a4})}{2} + \frac{(\rho_{a3} + \rho_{a1})}{(2)^{\frac{1}{2}}}\right]\left[\left(2 + (2)^{\frac{1}{2}}\right)\right] \quad \text{2.12d}$$

where $\rho_{a1}, \rho_{a2}, \rho_{a3}, \rho_{a4}$ are constitute resistivity values from the crossed square data.

2.3.1.3 Anisotropy sensitivity

To understand the sensitivity of the deployed array to the rock anisotropy, it was necessary to first calculate the apparent anisotropy (λ) and the bedrock anisotropy (N).

$$N = \left[\frac{(T+S)}{T-S}\right]^{\frac{1}{2}} \quad \text{2.13}$$

where; $T = A^{-2} + B^{-2} + C^{-2} + D^{-2}$ 2.13a

$$S = 2\left[\left(A^{-2} - B^{-2}\right)^2 + (D^{-2} - C^{-2})^2\right]^{\frac{1}{2}} \quad \text{2.13b}$$

and A, B, C and D are as defined in equation 2.12.

Apparent anisotropy is given by the ratio of apparent resistivity measured perpendicular to fracture strike to apparent resistivity measured parallel to fracture strike.

$$\lambda = \frac{\rho_{at}}{\rho_{a1}} = \frac{N\left[\left(N^2+1\right)^{\frac{1}{2}}-1\right]}{\left[\left(N^2+1\right)^{\frac{1}{2}}-N\right]} \quad \text{.....2.14}$$

where ρ_{at} is Apparent resistivity measured perpendicular to strike, ρ_{a1} is Apparent resistivity parallel to fracture strike, N is effective vertical anisotropy.

2.3.2 Gravity Method

This section explains the basic theory applied in gravity method. Gravity method depends on two laws derived from Newton's law. The laws are namely: Universal law of gravitation and the Newtons second law of motion. The Universal law of gravitation states that, the force of attraction between two bodies of known masses is directly proportional to the product of the Mass (M) of the Earth and mass *(m)* and inversely proportional to the square of the distance between their centers of mass (R).

$$F = \frac{GMm}{R^2} \quad \text{.....2.15}$$

where G is the gravitational constant and its value is $(6.67)10^{-11} Nm^2 kg^2$.

From second Newton's law of motion: The force (F) is equal to mass (m) multiplied by the acceleration. In case the acceleration acts in a vertical direction, then it is said to be due to gravity.

$$F = mg \quad \text{.....2.16}$$

Upon combining equation 2.15 and 2.16, we get,

$$MF = \frac{(GMm)}{R^2} = mg \quad \text{……..2.17}$$

Upon rearranging equation 2.17, we end up with equation 2.18, which shows that, magnitude of acceleration due to gravity on earth (g) is directly proportional to the Mass (M) of the Earth and inversely proportional to the square of the Earth's radius (R).

$$g = \frac{GM}{R^2} \quad \text{…….....2.18}$$

Ideally, the acceleration due to gravity is supposed to be constant over the entire earth for constant R. However, this is not always the case because of variations in the Earth's gravitational field due to several geological features. Therefore, raw gravity data obtained is normally subjected to drift, latitude, free air, bouguer slab and terrain corrections to reduce the observed data. The goal of gravity reduction is to correct for all variations in the Earth's gravitational field, which do not result from the differences of density in the underlying rocks.

2.3.2.1 Drift correction

In gravity survey, observed gravity values change as a function of time at a given location. The changes are due to instrument drift, and in some cases real changes for instance, motions on faults and swelling of magma chambers. Drift correction is carried out by drawing a curve of base station readings against time as shown via schematic diagram in Fig 2.4. It is assumed that drift curve is continuous and linear for two consecutive readings. Base station data is taken as the first and the last reading during each survey day to make sure that every other station reading taken can be located within the drift curve. The drift (d) for each station is either added or subtracted from the station reading depending on the side of the curve it falls.

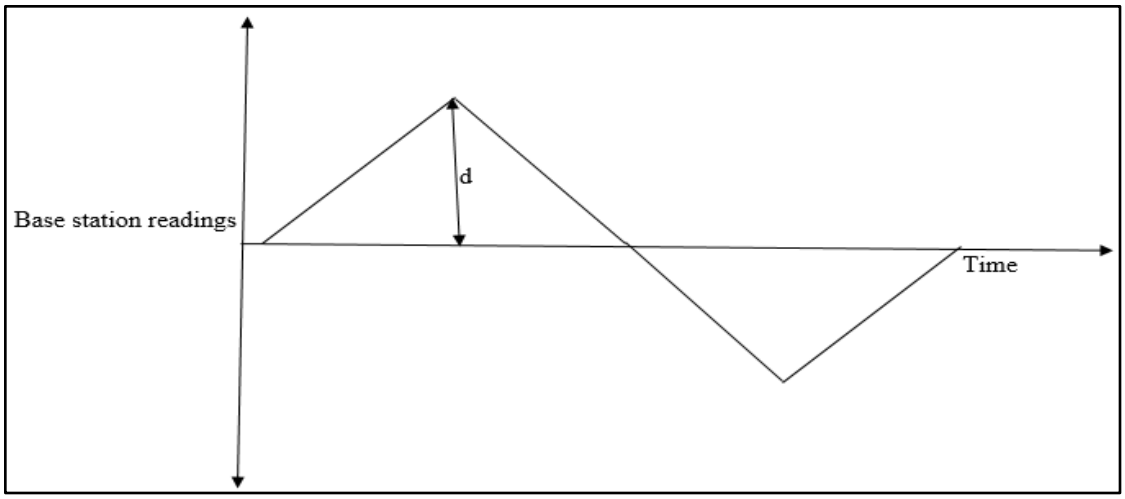

Figure 2.4: A Schematic graph of base station readings against time

2.3.2.2 Latitude correction

Latitude Correction (LC) account for Earth's elliptical shape and rotation. The earth's poles are closer to the center of the Earth than at the equator. However, there is mass under the equator and an opposing centrifugal acceleration, which is greater at the equator than at poles. The net effect is that gravity is greater at the poles than at the equator. For values relative to base station, gravity increases towards the Norths and so value obtained as in equation 2.19 is subtracted for the stations located along the Northern side of the base station (The 'a' is latitude) (Murty & Raghavan, 2002).

$$LC = 0.811\sin(2a) \text{ mgal} \quad \text{……………………………………………………2.19}$$

2.3.2.3 Free air correction

Free-air correction (FAC) accounts for gravity variations caused by elevation differences in the observation locations. This correction does not account for the effect of mass between the observed point and the datum. FAC is calculated as follows;

$$\Delta gfac = 0.3086h \text{ mgal} \quad \text{……………………………………………………2.20}$$

FAC Correction is added for stations above the datum and subtracted for stations below the datum.

2.3.2.4 Bouguer Slab Correction

Bouguer Slab Correction is a first order correction and accounts for the excess mass underlying observation points located at elevations higher than the elevation datum (sea level or the geoid). Conversely, it accounts for the mass deficiency at observation points located below the elevation datum.

$$\Delta gb = -0.04193\rho h \text{ mgal} \quad \text{.....2.21}$$

where ρ is average density of the rocks underlying the survey area. Bouguer correction is subtracted for stations above the datum and added for stations below the datum (Murty & Raghavan, 2002).

2.3.2.5 Terrain correction

Terrain correction accounts for variations in the observed gravitational acceleration caused by variations in topography near the observation point. This correction is carried out manually by use of a "Hammer chart and a topographic map as illustrated in Figure 2.5.

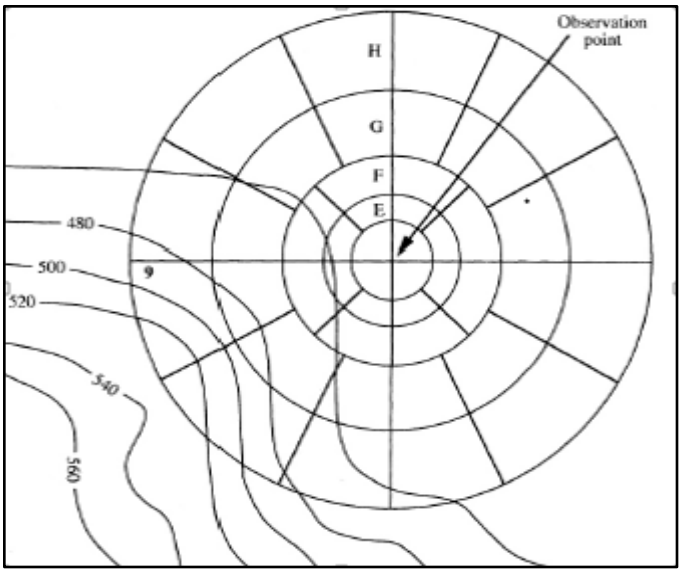

Figure 2.5: Hammer chart (Hammer, 1939)

Because of the assumptions made during the Bouguer Slab correction, the terrain correction of a compartment T is positive regardless of whether the local topography consists of a mountain or a valley.

$$T = 0.4191\frac{\rho}{n}\left(r_2 - r_1 + \sqrt{r_1^{\,2} - Z^2} - \sqrt{r_2^{\,2} - Z^2}\right) \ldots\ldots\ldots\ldots\ldots\ldots\ldots\ldots\ldots\ldots\ldots\ldots 2.22$$

where ρ is the bouguer Correction density (Mgm^{-3}); n is the number of compartments in zone; r_1 inner radius of zone (m); r_2 outer radius of Zone (m) ; and Z is the Modulus of elevation difference between observation point and mean elevation of compartment(m) (Chandler,1994). In this research, theoretical concept was useful in computing physical parameters, which were later analyzed to give the survey results.

CHAPTER THREE

MATERIAL AND METHODS

3.1 Introduction

This chapter involves description of data collection procedure and processes involved in data analysis for both geo-electrical resistivity and gravity techniques. Since the focus in this study is evaluation of groundwater potential, the procedures described were tailored to help achieve the research objectives. In this survey, SSR-MP-ATS resistivity meter model was used in taking resistivity data. This equipment injects electric current into the subsurface through a pair of conducting electrodes. It automatically computes and displays the apparent resistivity value from potential difference created in the subsurface by the injected current. The potential difference is measured by an in-built potentiometer. Other parameters that SSR-MP-ATS resistivity meter model display include the injected current value, measured potential difference and voltage status of the battery.

3.2 Resistivity data collection

Azimuthal square array configuration was deployed in this research. Two current electrodes namely A and B were used together with other two potential electrodes M and N. These electrodes were placed at the corners of a square of side ("a") and measurement point was assigned to the center of the square. The depth of investigation was approximately equal to the length of the square (a). Starting with N-S electrode alignment the electrodes were connected to the corresponding resistivity meter terminals and three readings that is $\rho_{a\alpha}$, $\rho_{a\beta}$ and $\rho_{a\gamma}$ were taken. The square formed was then collapsed and rotated at various angles. The first square was set and rotated through 30^0 increments up to 360^0 about the center of the square. The resistivity data was taken for various values of ("a") on each targeted direction. The rotations covered a maximum of

360^0 from the starting azimuth. Fifteen pecks and a geometric protractor were used in setting up each survey station (Figure 3.1).

Figure 3.1: Survey station Azimuth set up

Along the east-west direction, twelve survey stations were established (see appendix) within the study area (Figure 3.2). For each station, northings, easting, and elevation measurements were taken using a handheld GPS.

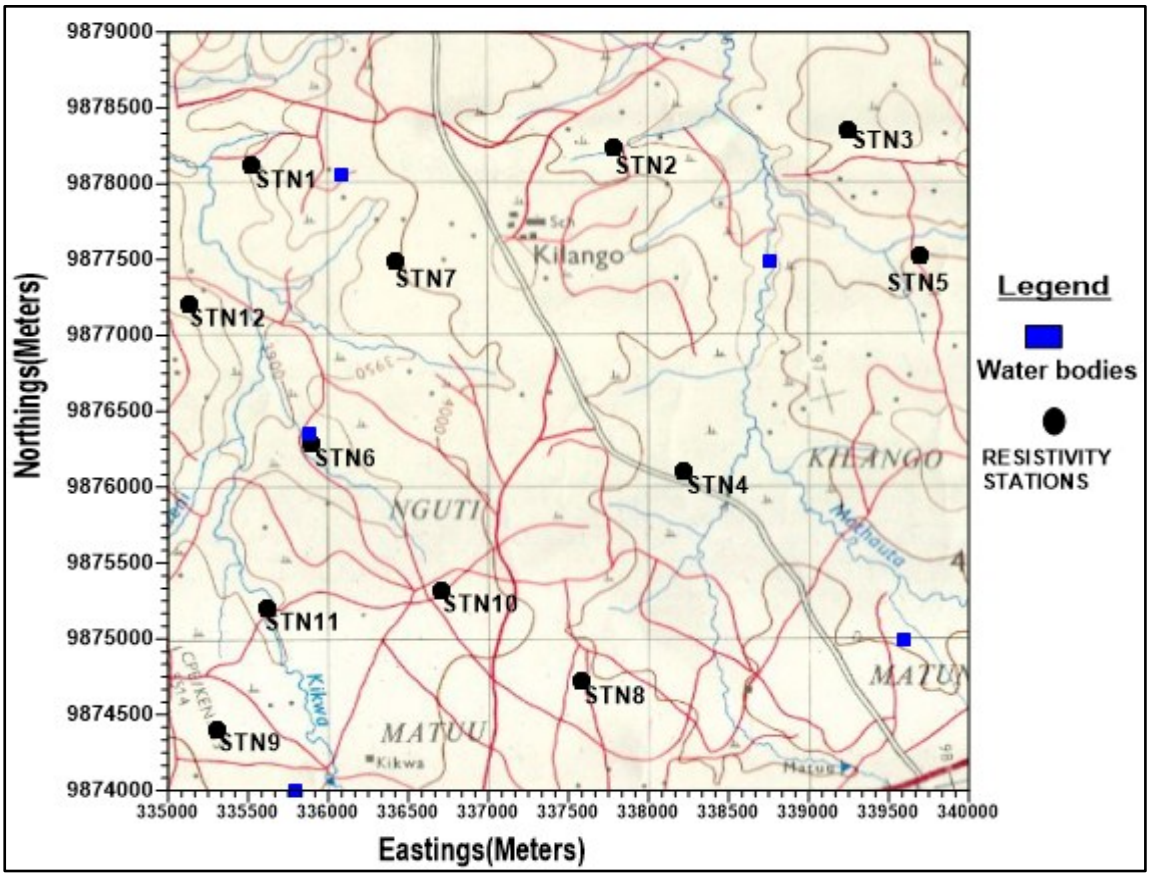

Figure 3.2: Resistivity station locations (Survey of Kenya, 2005)

3.2.1 Resistivity Data Processing

Data obtained was quantitatively analyzed and used in drawing Geometric resistivity polar charts (Figure 4.2). The geometric resistivity values observed along the suspected secondary fractures for each station were contoured to help understand the resistivity distribution within the area. From the collected geometric resistivity data, crossed square array data was calculated and used in analysis.

3.3 Water conductivity data

Water conductivity meter was used in collecting water conductivity readings from five subsurface water bodies (see appendix) located within the study area (Figure 3.2). Using water conductivity measurements and the resistivity data it was possible to calculate the porosity data for each station.

3.4 Gravity data collection

There are two types of gravimeters: absolute and relative. Absolute gravimeters measure the local gravity in absolute units ("Gal" after "Galileo"). Absolute gravimeters are compact and an example of such is the Autograv CG-5 model. It works by directly measuring the acceleration of a mass during free fall in a vacuum. The accelerometer is rigidly attached to the ground.

Relative gravimeters are spring based. It is a specially assembled extremely sensitive spring balance carrying a fixed mass. The basic principle is that changes in gravity result to a change in weight of fixed mass upon a change in location. During any gravity survey, the gravimeter is calibrated at regular interval at a base station where the absolute value of gravity is known. Absolute gravity values at survey stations are obtained by reference to the International Gravity Standardization Network (IGSN). A commonly used instrument for taking gravity measurements and the one that was used in this research is Worden gravimeter (Figure 3.3).

Figure 3.3: Worden Gravimeter (Dobrin &Savit, 1960)

It is a compact temperature-compensated gravimeter with precision level less than 0.1 mgal. The system is held in unstable equilibrium about an axis.

In this survey, one hundred and fifty six gravity stations including the base stations were established (see appendix) using a handheld Global Positioning System (GPS). A control station close to the study area was located using the International Gravity Standardization Network (IGSN). Across the study area six transects were ran covering 5km distance each in east-west direction to make sure every present fault or fracture is detected (Figure 3.4). At first, a base station was established and was re-occupied after every one hour. Data obtained from the base station was used during data processing to account for the instrumental drift.

The gravity stations established had a separation distance of 200 meters distance from each other to enable detection of narrow faults/fractures. The six transects established had a separation distance of 1km from each other. For each station, gravity meter reading, Elevation and time at which each reading was taken were recorded. During the survey period, base station reading was taken as the first and as the last measurement of each day.

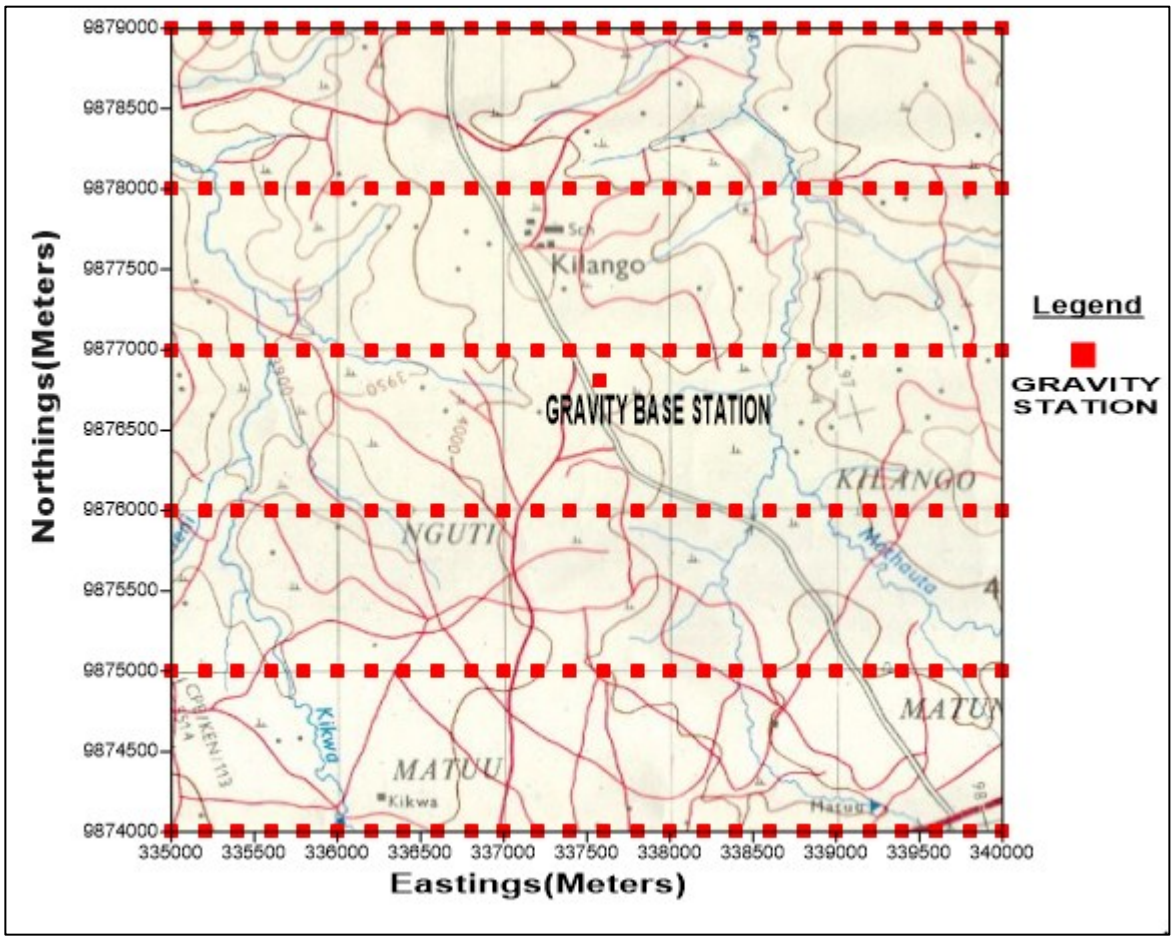

Figure 3.4: Gravity survey stations location

3.4.1 Gravity Data Processing

Raw gravity data obtained was subjected to corrections to reduce the observed data to a common datum. After correction, the acquired data was processed for effective interpretation of the subsurface faults and fractures that are potential fluid conduits. The major corrections carried out on the absolute values of the gravitational field were, drift, latitude, free air, bouguer slab and terrain.

Drift curves of base station readings against time for each day were drawn (Figure 3.5). It was assumed that each drift curve generated was continuous and linear for two

consecutive readings. The drift (d) for each station was either added or subtracted from the station reading depending on station location.

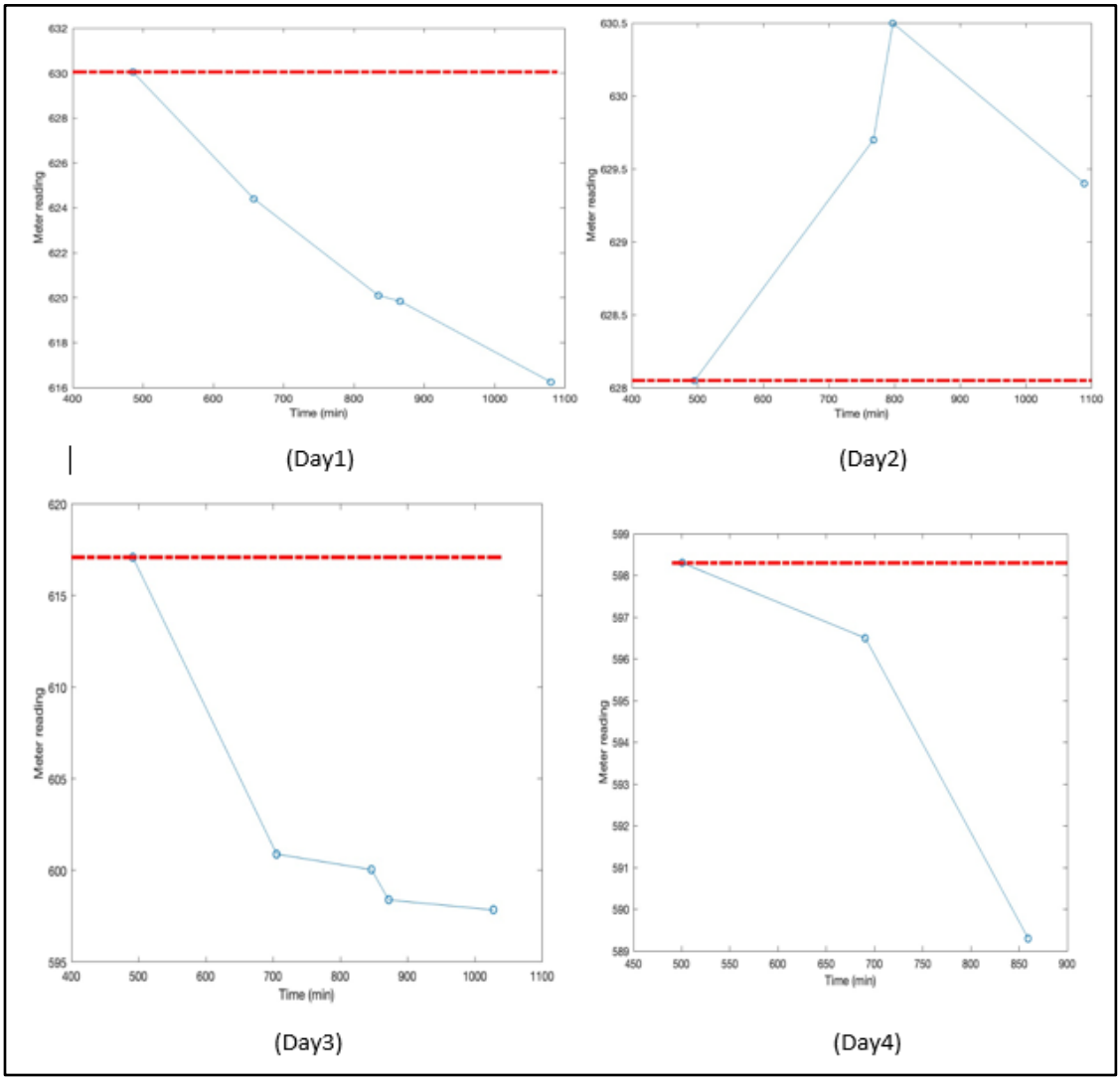

Figure 3.5: Graph of base station readings against time

Latitude Correction accounted for Earth's elliptical shape and rotation. Gravity increases towards the Northside, so value obtained from equation 2.19 was subtracted for the value located along the Northern side of the base station. Free-air correction was calculated using equation 2.20. FAC Correction was added for stations which were

located above the datum and subtracted for stations below the datum. Bouguer Slab Correction is a first order correction and was calculated using equation 2.21. Terrain correction was calculated using equation 2.22. Terrain correction involved the use of a "Hammer chart" and a topographic map. Performing these corrections was paramount in order to determine gravity anomalies caused solely by the local subsurface structures. Using the corrected gravity values, a complete bouguer anomaly contour map was generated using Surfer 10 software. The Euler software was used in plotting cross-section AA' imaging the subsurface structures within the region. Using Grav2dc software, 2D model was used in forward modeling to determine the density values of the anomalous structure.

CHAPTER FOUR

RESULTS AND DISCUSSION

4.1 Introduction

This chapter presents a brief explanation on how softwares were utilized, discussion of results obtained from the data processing and analysis outlined in chapter two. This was achieved with the aid of tables, figures and maps. The main topics in this chapter include; the resistivity measurement control, results from azimuthal square array data analysis, and comprehensive discussion of results obtained from calculated geo-electric and gravity parameters. This aim at identification of groundwater primers and determination of inferred aquifer characteristics as far as groundwater potential evaluation in Matuu region is concerned.

4.2 Software overview

In data processing Surfer 10, 2D Euler deconvolution software and Grav2dc software were utilized. Surfer 10 program was used for qualitative analysis of both geo-electrical and gravity data. Using Kriging technique, a geo-statistical gridding method, surfer software was used in generating both geometric resistivity and complete bouguer anomaly contour maps. Surfer 10 software was used to interpolate the original resistivity and gravity data to express the trends portrayed using gridding methods based on equation 2.1.It was also used in overlaying the digitized topographic map of the area, the geometric resistivity, porosity and complete bouguer anomaly contour layers.

2D Euler deconvolution softwares by least squares method generated a horizontal gradient with profile data, inclination, declination, flight height, structural index and background normal total gravitational field as input. 2D Euler deconvolution software was used in creating models of discontinuity on the faulted/fractured based on Euler's homogeneity equation 2.2. Grav2dc software was used in modelling the residual

complete bouguer anomaly data from cross-section AA' to provide a better understanding of the causative bodies geometry and density contrast.

4.3 Azimuthal square array

Apparent resistivity was computed using equation 2.10 and used in calculating the bedrock anisotropy and the apparent anisotropy. The calculated parameter were tabulated (Table 4.1) and a graph of apparent anisotropy against bedrock anisotropy was plotted (Figure 4.1).

Table 4.1: Apparent anisotropy and the bedrock anisotropy data

STATIONS	λ (apparent anisotropy)	N (bedrock anisotropy)
STN1	10.1632	1.9821
STN2	11.4000	2.0515
STN3	9.35829	1.9339
STN4	10.6249	2.0087
STN5	8.0338	1.8478
STN6	11.1438	2.0376
STN7	10.5836	2.0063
STN8	40.1964	3.0051
STN9	65.6362	3.4944
STN10	15.6184	2.2550
STN11	16.9343	2.3107
STN12	12.3285	2.1002

The plotted anisotropy graph (Figure 4.2) provided a clear understanding of the anisotropism of the bedrock in the region. It also showed a high upward trend and a significant change in the apparent anisotropy, which resulted to a slight change in bedrock anisotropy. This justified that Azimuthal Square Array Configuration is more

sensitive to the bedrock anisotropy, which was an advantage because the measured apparent resistivity was less likely to be obscured by the overburden. High anisotropy detected showed that the bedrock rock formation within the region was asymmetrical and probably aligned in different directions.

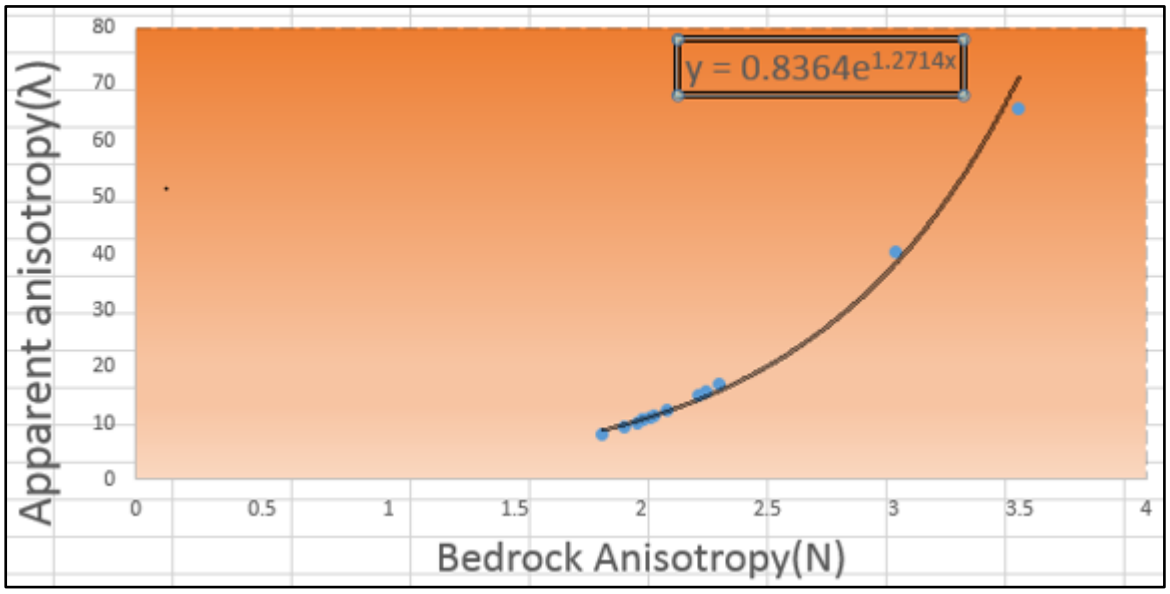

Figure 4.1: A graph of apparent anisotropy against bedrock anisotropy

4.3.1 Polar plots

The apparent resistivity data was utilized in plotting azimuthal polar plots (Figure 4.2), which displayed several fracture orientations within the study area.

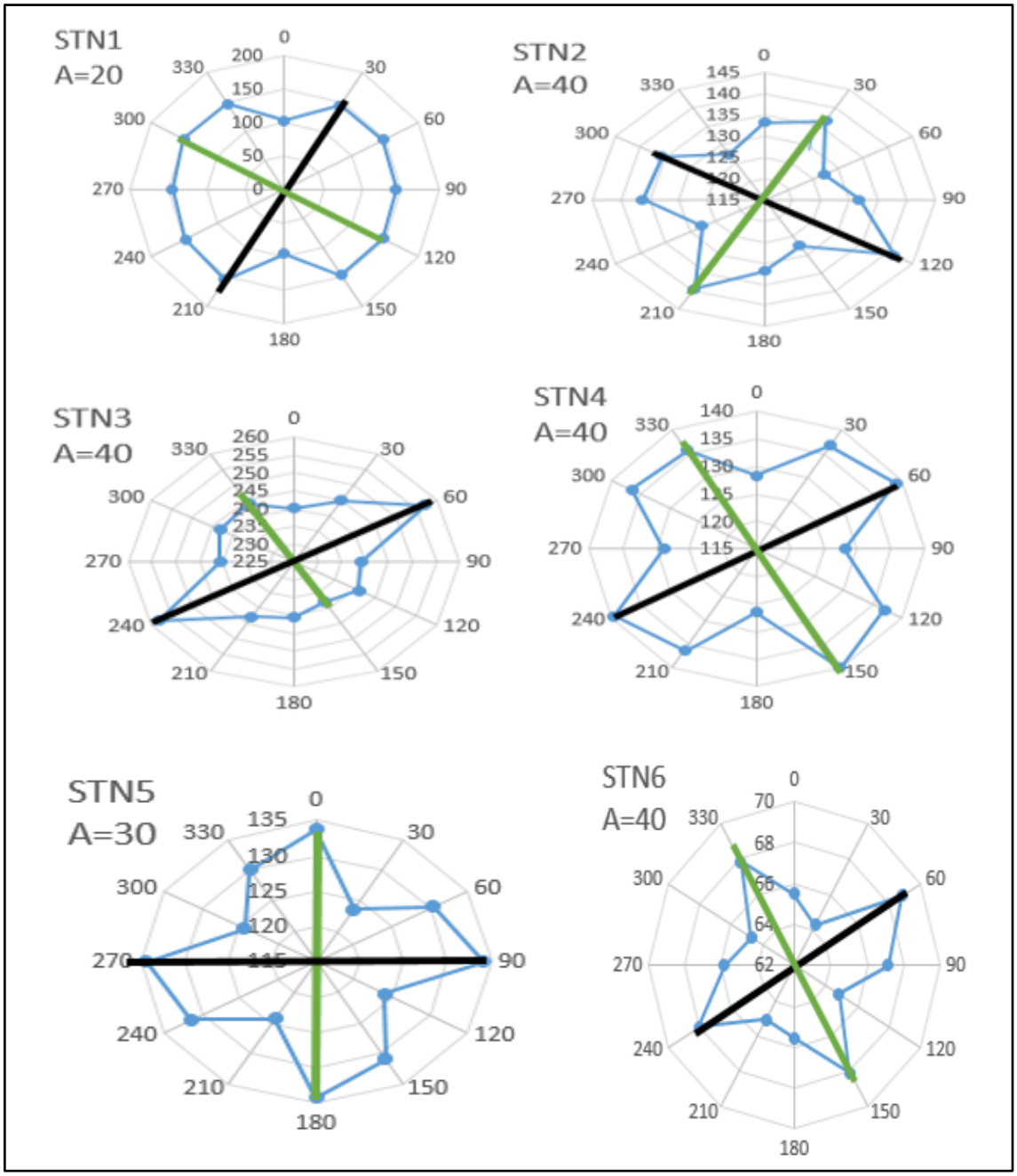

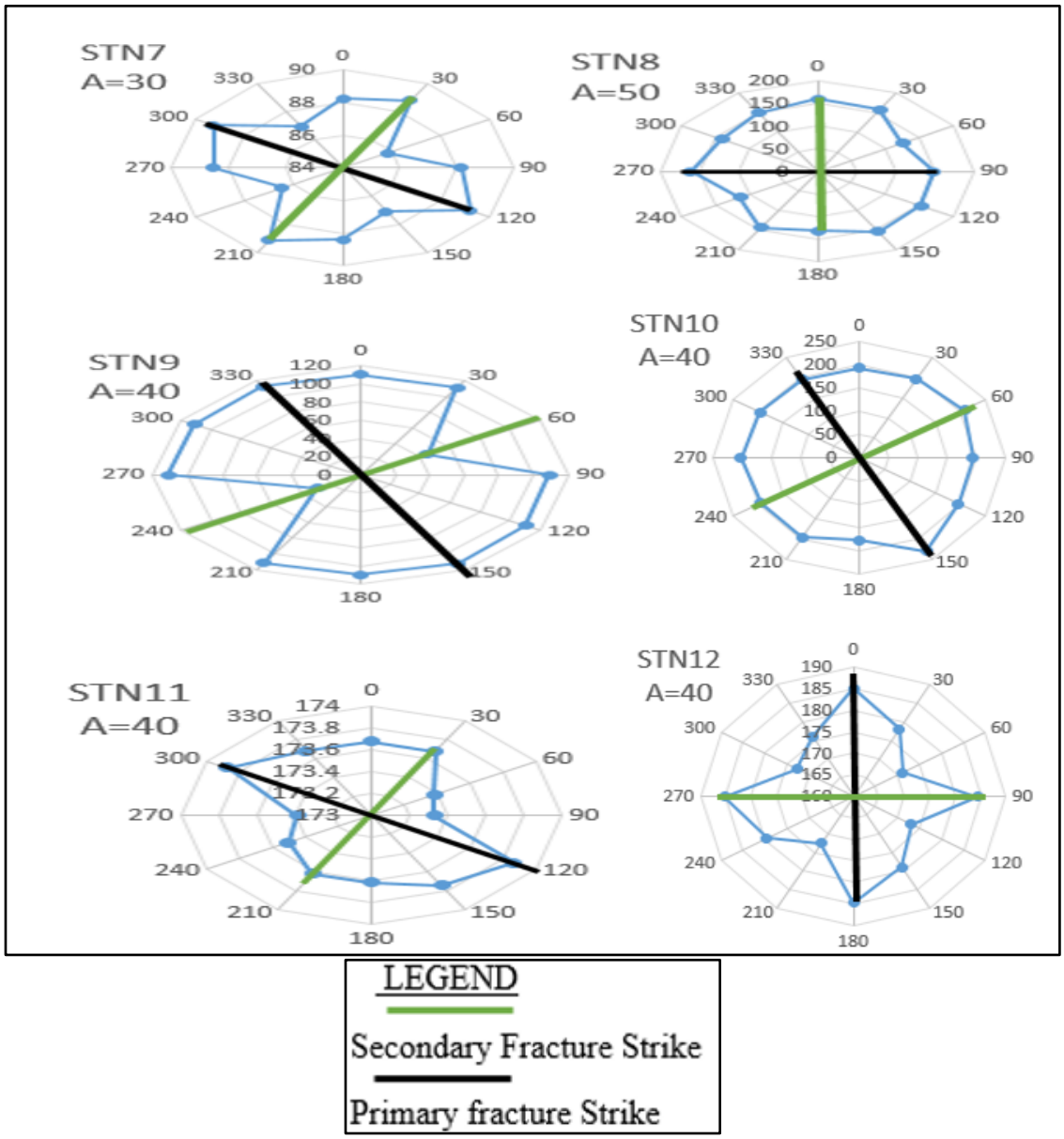

Figure 4.2: Azimuthal polar plots

In a polar plot, a fracture strike orientation is said to be along the azimuth, which is perpendicular to the azimuth with maximum resistivity values (Lane et al., 1995). Each survey station displayed a possibility of a fracture strike along a particular orientation. The geometric apparent resistivity values along all the fracture strike azimuths were

tabulated (Table 4.2) and utilized in generating geometric apparent resistivity contour map using Surfer 10 software (Figure 4.3).

Table 4.2: Geometric resistivity data

STATIONS	EASTINGS	NORTHINGS	GEOMETRIC RESISTIVITY VALUE Ωm
STN1	335515	9878124	99.2035
STN2	337787	9878242	137.9242
STN3	339249	9878351	240.9757
STN4	338225	9876102	139.1694
STN5	339691	9877525	134.0131
STN6	335895	9876291	67.9703
STN7	336425	9877486	88.9634
STN8	337587	9874717	119.8855
STN9	335301	9874396	36.6640
STN10	336710	9875323	200.8740
STN11	335615	9875204	173.6445
STN12	335132	9877212	175.3316

Geometric resistivity contour map generated (Figure 4.3) displayed five distinct regions.

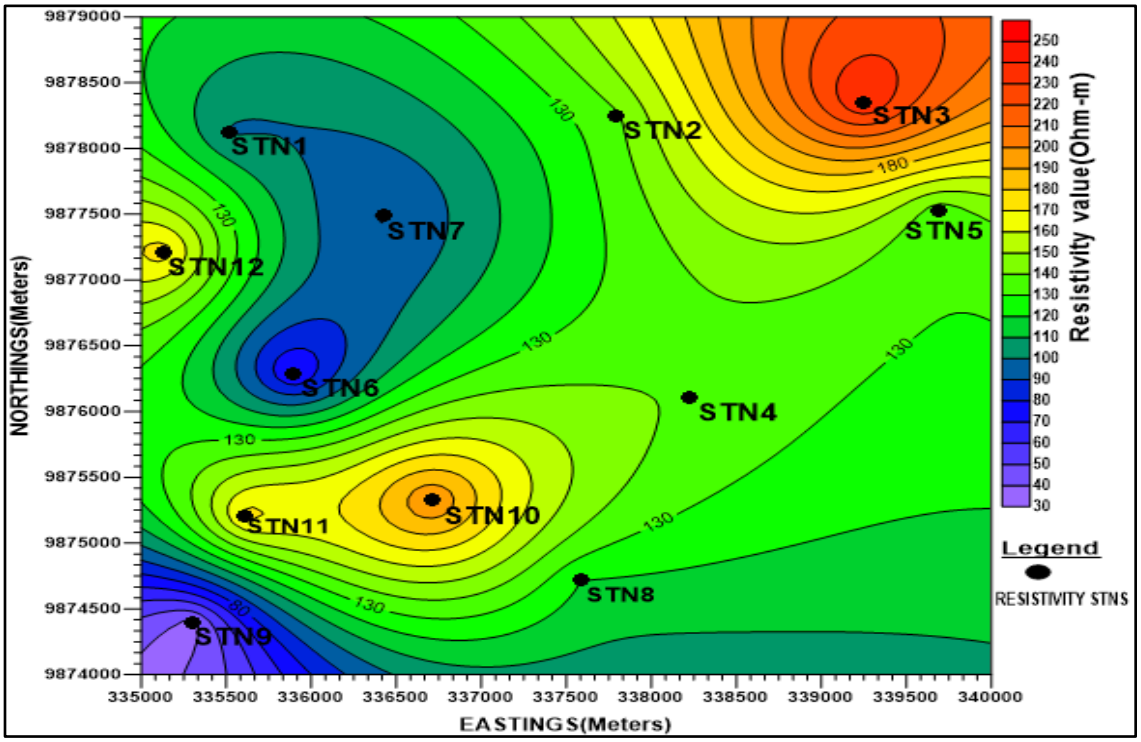

Figure 4.3: Geometric Apparent Resistivity contour map

Towards the northeastern part of the study, a substance with very high resistivity values ranging from 200 to 250 Ωm was detected. Second region was represented with the yellow color and the resistivity values for this region ranged from 160-190 Ωm. The third region was the part with the green color. This region displayed resistivity values ranging from 100 to 150 Ωm. The forth region had blue color with resistivity values ranging from 50-90 Ωm. This was the zone of interest in this study because the same area showed presence of a low-density substance. The fifth zone of interest was the part represented with purple color. This region has very low resistivity values ranging from 30-40 Ωm compared to the rest of the regions displayed.

4.3.2 Fracture strike orientation

Fracture strike orientation was both graphically and analytically determined using geometric resistivity, porosity and crossed square array data.

4.3.2.1 Graphical method

In each Polar chart an azimuth along which the fracture strike was suspected to be oriented along was determined and categorized as shown in Table 4.3. Graphically, the main fracture within the study area was found to be oriented along NE-SW direction (Table 4.4 and Figure 4.4).

Table 4.3: Estimated fracture strike azimuth

STATIONS	POI	FRACTURES STRIKE AZIMUTH
STN1	20	0-180
STN2	40	30-210
STN3	40	150-330
STN4	40	60-240
STN5	30	0-180
STN6	40	150-330
STN7	30	30-210
STN8	50	60-240
STN9	40	60-240
STN10	40	60-240
STN11	40	30-210
STN12	40	60-240

Table 4.4: A fracture strike orientation frequency distribution table

FRACTURE STRIKE ORIENTATION	FREQUENCY
N-S	1
NE-SW	8
E-W	0
NW-SE	3

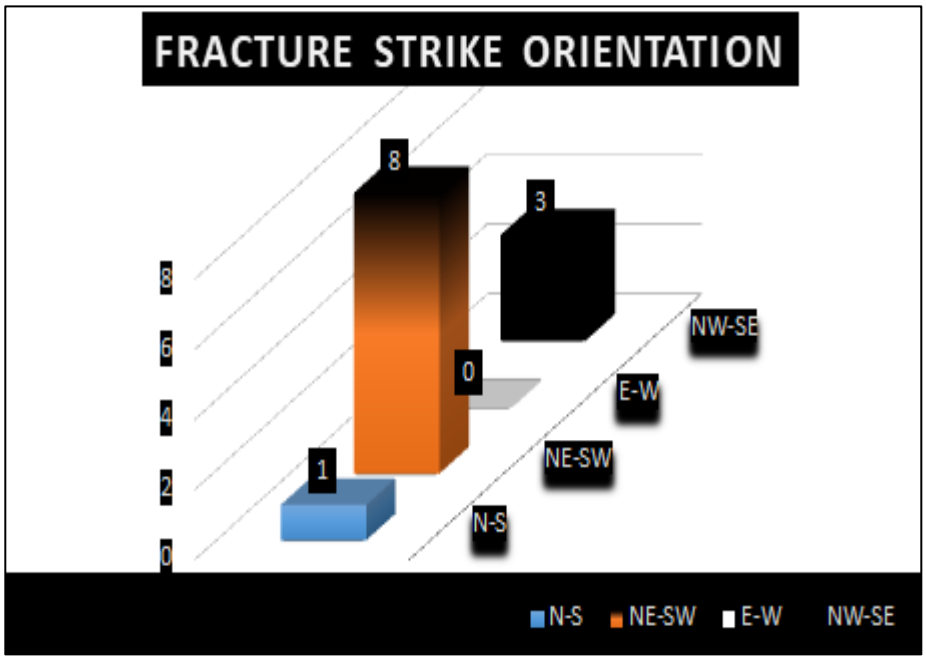

Figure 4.4: Graphical representation of the fracture strike orientation

2.3.2.2 Geometric resistivity data

The geometric apparent resistivity data was contoured (Figure 4.3) and nine cross-sections were drawn across the anomalous region-using surfer 10 software (Figure 4.5).

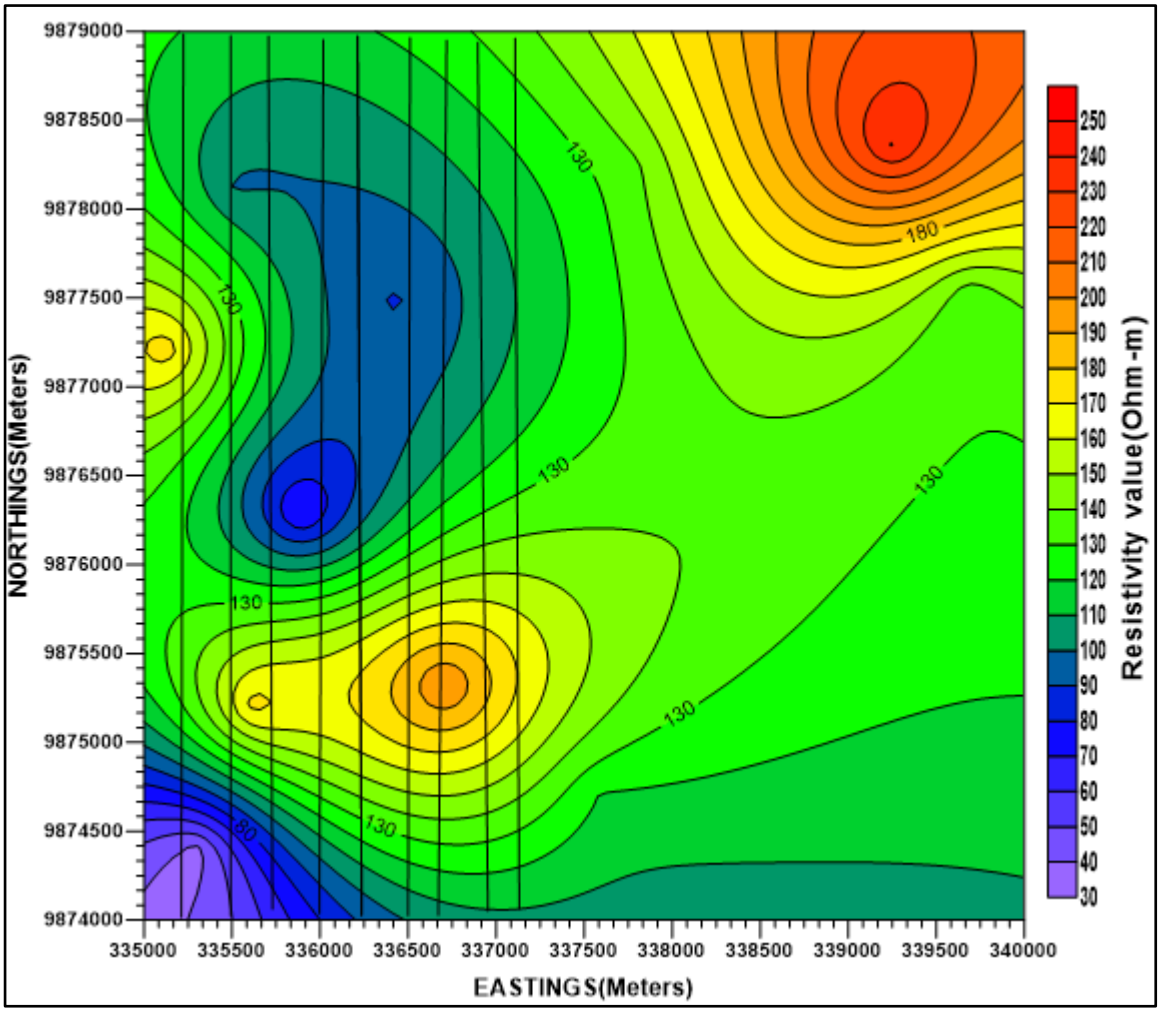

Figure 4.5: The Nine cross-sections drawn across the geometric resistivity anomalous zone

Data from these cross-sections was used in marking the orientation of the main fracture within the study area. Using this approach, resistivity method displayed a fracture strike along NE-SW direction (Figure 4.6).

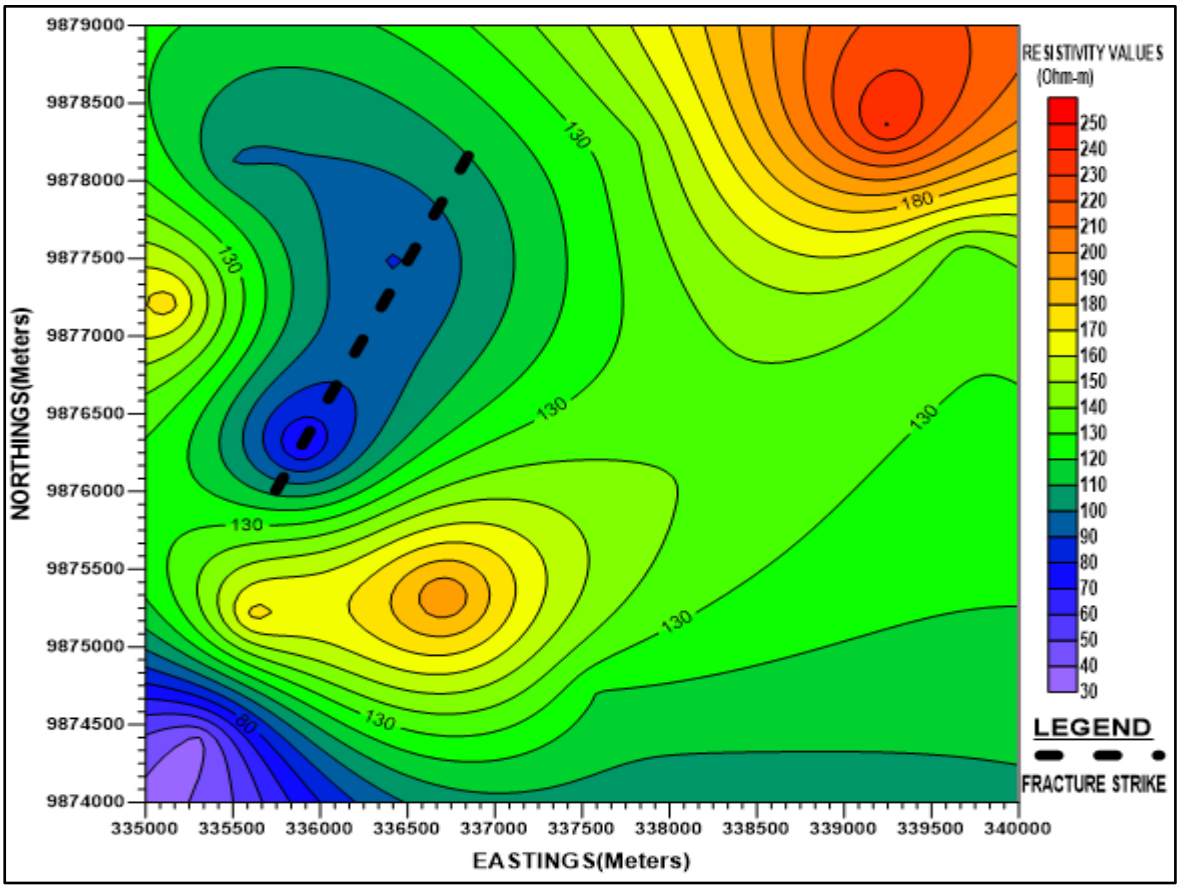

Figure 4.6: Inferred fracture strike orientation on the geometric apparent resistivity contour map

2.3.2.3 Porosity data

Water conductivity data (Table 4.5) obtained was utilized in generating water conductivity contour map (Figure 4.7).

Table 4.5: Water conductivity data

Northings	Eastings	WATER CONDUCTIVITY($\mu S/cm$)
9876351	335877	281
9877490	334758	136
9874063	334077	163
9874000	335800	111
9875000	339600	221

Water conductivity reading for each resistivity station was determined from the conductivity contour map. To achieve this, a conductivity contour map was generated (Figure 4.7), and then resistivity layer was posted in the map from which it was possible to obtain water conductivity values for each resistivity station.

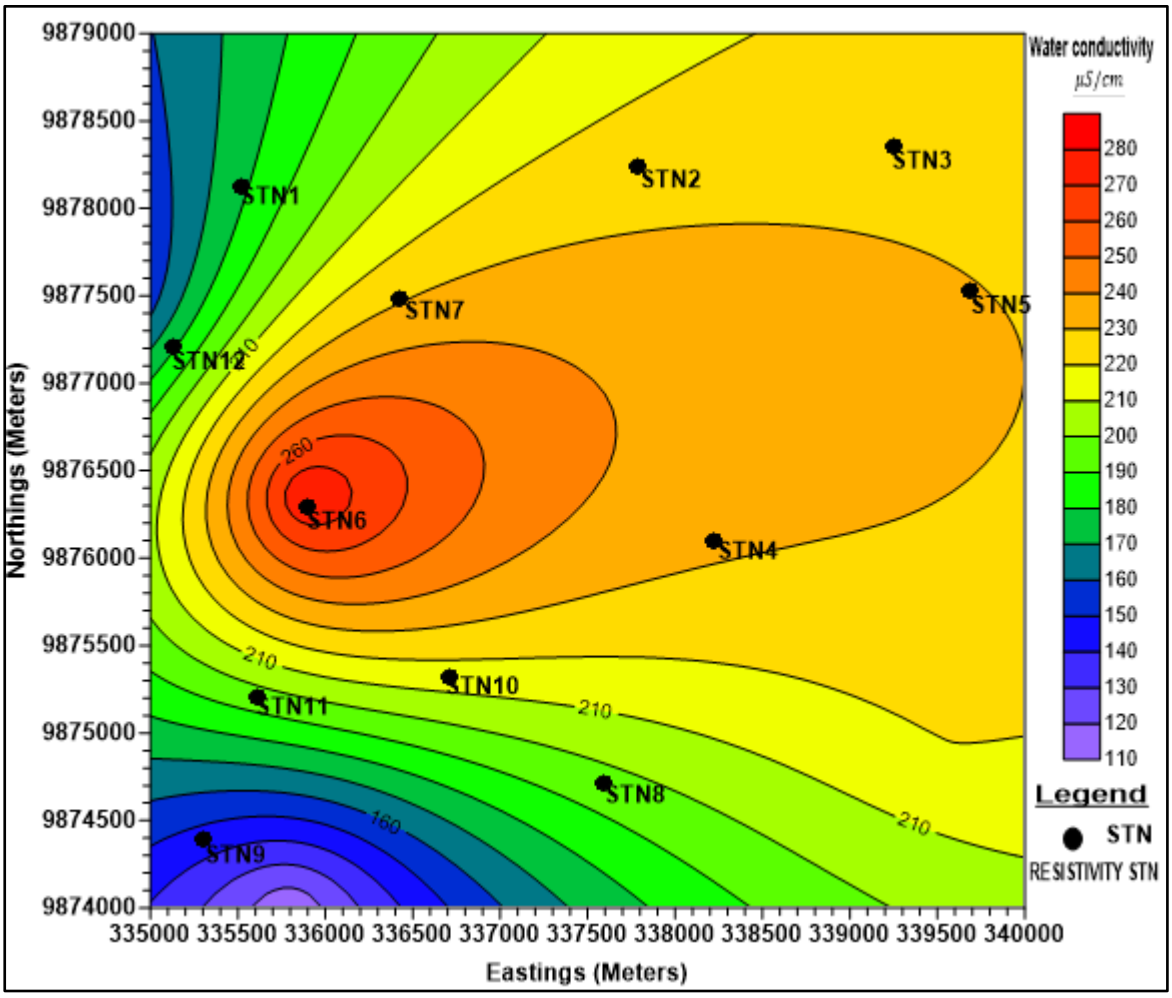

Figure 4.7: Water conductivity contour map

Conductivity readings for all the resistivity stations were tabulated and used in calculating porosity values for all resistivity stations.

Water resistivity data (R_w) was computed from the water conductivity measurements obtained. This was done by getting the reciprocal of the conductivity measurement values. Porosity values for each survey station were calculated from the resistivity values of the formation (R_t) and the water resistivity data (R_w) using equation 4.1 (Table 4.6).

Table 4.6: Resistivity formation (R_t) and the water resistivity data (R_w)

STN	EASTINGS	NORTHINGS	R_t	R_w
STN1	335515	9878124	99.2035	53.0767
STN2	337787	9878242	137.9242	58.3368
STN3	339249	9878351	240.9757	101.0860
STN4	338225	9876102	139.1694	57.2151
STN5	339691	9877525	134.0130	55.4586
STN6	335895	9876291	67.9703	23.3282
STN7	336425	9877486	88.9634	37.3013
STN8	337587	9874717	119.8855	57.8587
STN9	335301	9874396	36.6640	23.6824
STN10	336710	9875323	200.8741	88.8439
STN11	335615	9875204	173.6445	83.9070
STN12	335132	9877212	175.3317	93.4863`

$$R_t / R_w = a\phi^{-m} \quad \text{.....4.1}$$

where (a) and (m) are constants and their values were 1 and 2 respectively, ϕ is the porosity.

The computed porosity data (Table 4.7) was then utilized in generating porosity contour map (Figure 4.8).

Table 4.7: Porosity data

EASTINGS	NORTHINGS	POROSITY VALUES (%)
335515	9878124	20.751450145232
337787	9878242	20.382168611537
339249	9878351	16.513914601248
338225	9876102	20.425643737959
339691	9877525	20.887025224327
335895	9876291	29.042234229866
336425	9877486	24.242475961847
337587	9874717	19.966031061962
335301	9874396	25.931371824653
336710	9875323	16.515821618523
335615	9875204	15.491727026361
335132	9877212	16.468755677338

The porosity data was contoured and nine cross-sections were drawn across the porous region (Figure 4.8).

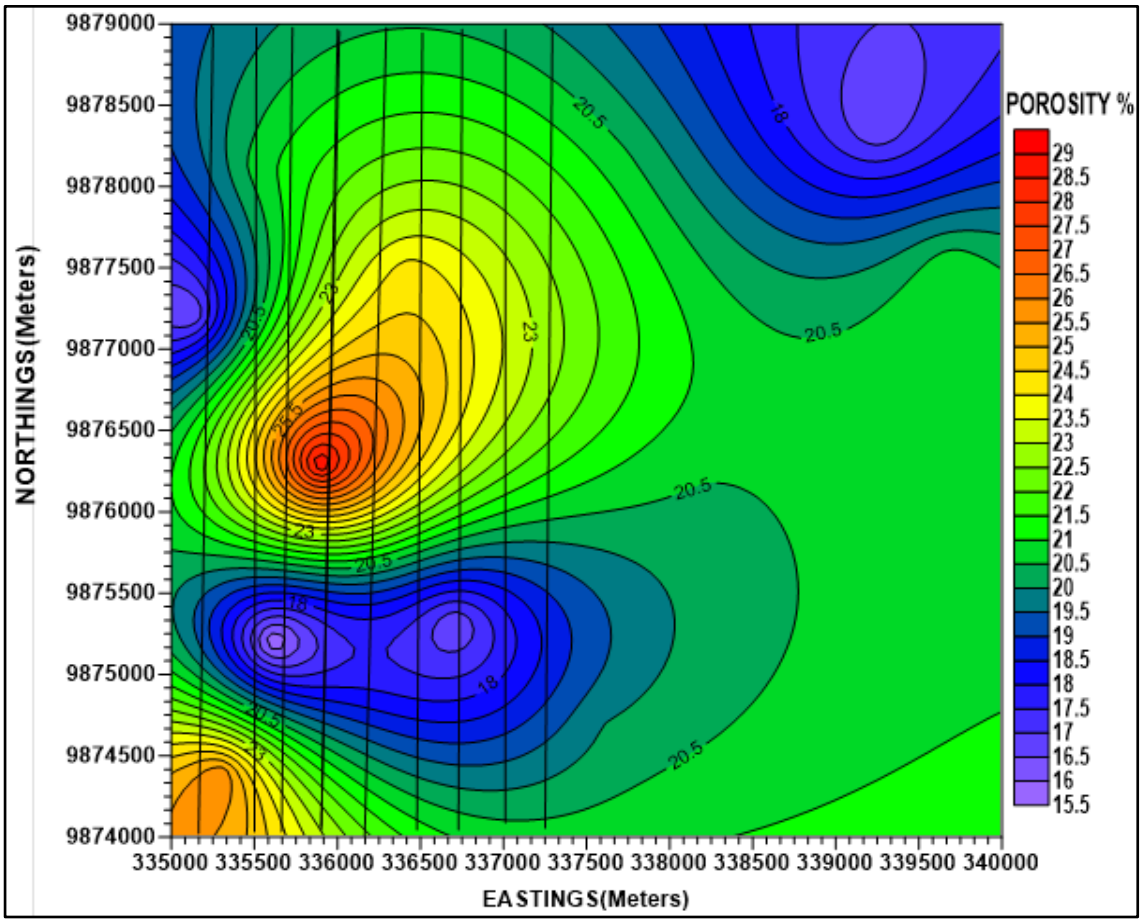

Figure 4.8: The Nine cross-sections drawn across the porous zone

Data from these cross-sections was used in determining the orientation of the main fracture within the study area. Using this approach, porosity data displayed fracture strike along NE-SW direction. This is shown in figure 4.9.

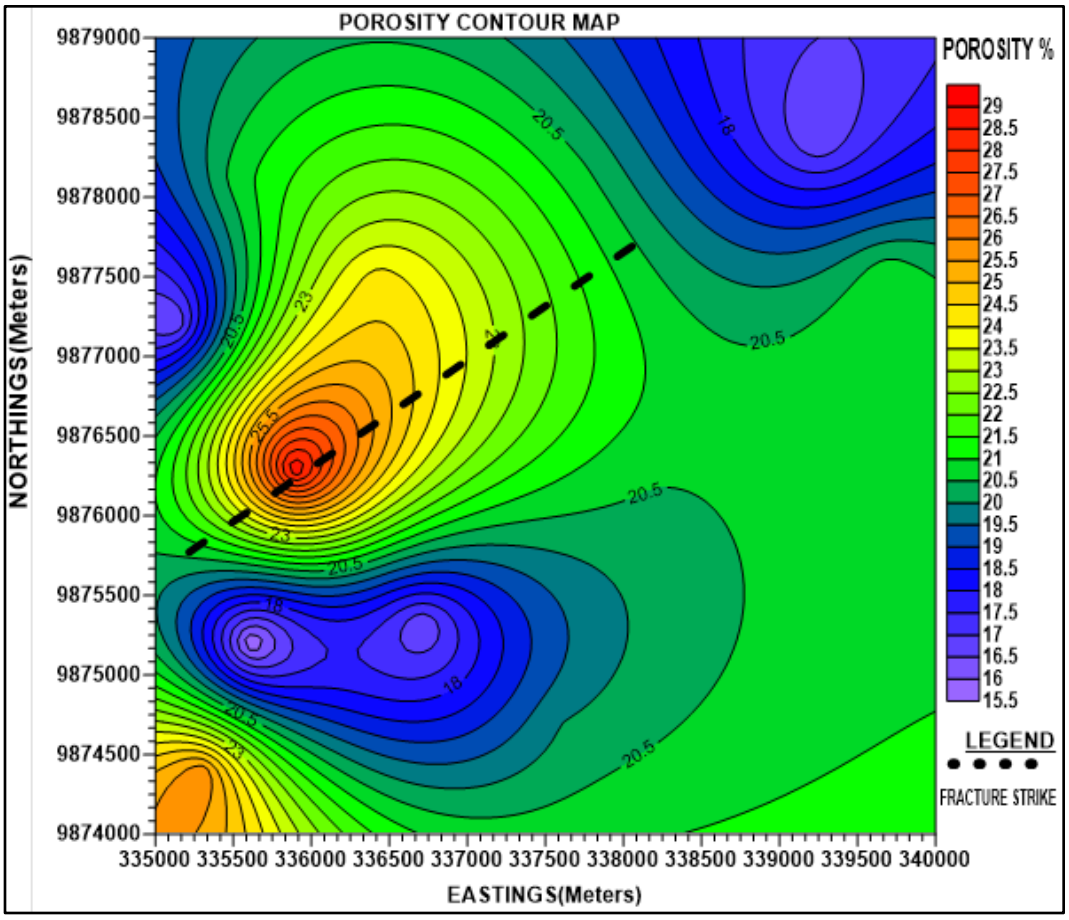

Figure 4.9: Inferred fracture strike orientation on the porosity contour map

The Geometric apparent resistivity and the porosity contour maps together with digitized topographic map of the study area were overlaid and zone of interest was delineated (Figure 4.10).

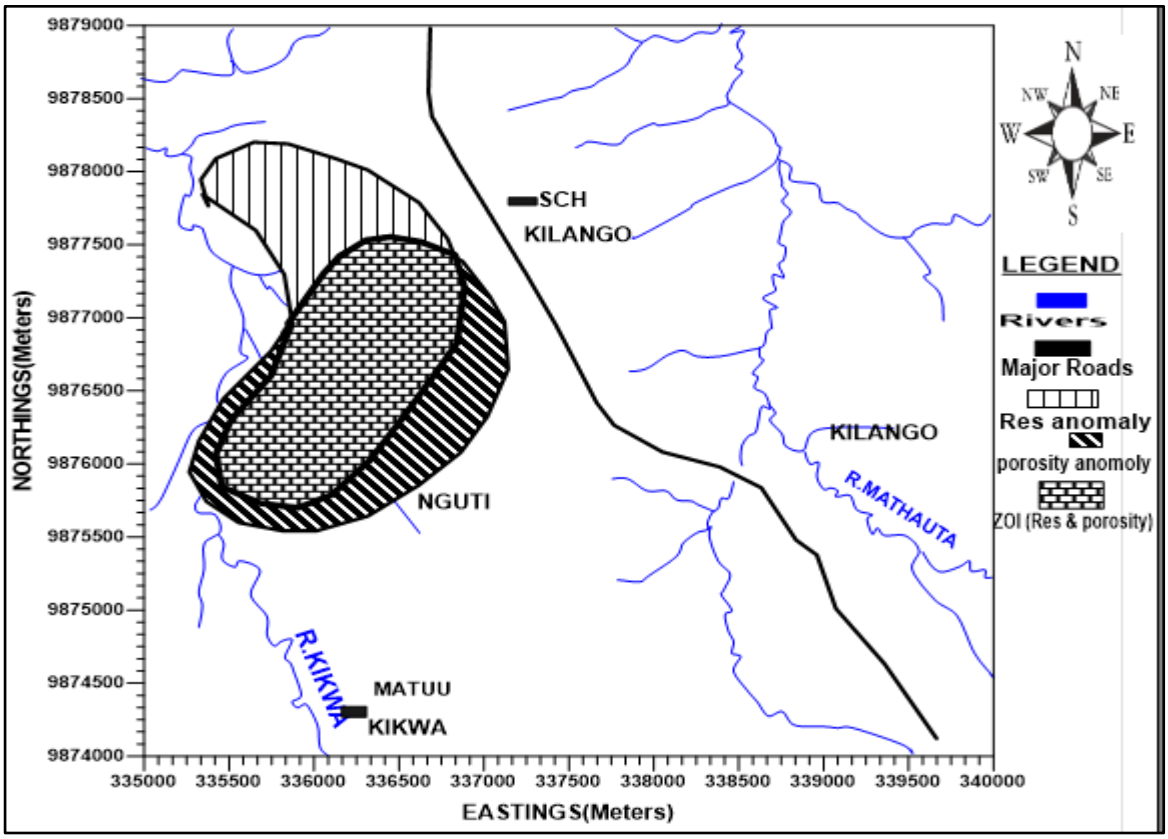

Figure 4.10: Map showing low resistive zone

2.3.2.4 Analytical method

Under this method, Crossed square data (Table 4.8) was utilized. Using equation 2.12, the fracture strike present in the area was found be oriented along 039.13245^0.

Table 4.8: Fracture strike azimuth from crossed square array

A	B	C	D	FRACTURE STRIKE (Θ)
1481.423828	1413.666025	1579.805337	149043.7868	41.8149
1666.048802	1505.84738	1706.993956	156658.6185	38.3804
3181.724584	2817.619876	3421.261899	522070.4672	36.1758
1697.781479	1494.185782	1765.703162	156530.2537	36.2609
1636.165608	1582.677237	1858.91156	142563.8358	42.4644
796.1222938	758.5734833	830.5368764	38680.09008	41.8483
1099.895737	1003.313398	1148.413024	67179.1744	38.7948
1732.750239	2036.461095	1656.890113	298260.4585	37.9172
1009.342766	1313.395834	991.0241646	96444.90609	34.2298
2292.435256	2319.699529	2257.333227	399031.7833	44.3509
2017.221748	2022.041745	1979.680282	301065.3487	44.8686
2139.901519	2584.861476	2606.978683	342177.8214	34.6903
Estimated fracture strike azimuth within the study area				39.3164

Discussion

Azimuthal Square Array Resistivity method was used to study resistivity within the bedrock region of Kilango Matuu area. Geological report of the study area showed that rocks of different physical properties along different directions dominate the region. In the first station, using "a"=20 meters length, the plotted polar chart displayed maximum apparent resistivity value along 030^0 resulting to a fracture strike along 0300^0 East. In survey station 2 using "a"=40 meters, the azimuthal polar plot showed maximum apparent resistivity along azimuth that was perpendicular to 030^0, the azimuth suspected to be the location where the fracture strike cuts across. In station 3 using "a"=40 metres,

a fracture strike was displayed along 0330^0 East. In station 4 using "a"=40 metres, maximum apparent resistivity was detected along 060^0 East which was perpendicular to 0330^0 and suspected to be the fracture strike orientation. In survey station 5 using "a"=30 metres a fracture strike was detected along 000^0 East. The polar plot generated form station 6 data using "a"=40 metres displayed maximum apparent resistivity along 060^0 East, an azimuth perpendicular to 330^0 East, the angle along which the fracture in the region was orientated along. In survey station 7 using "a"= 30 metres the fracture strike was suspected to be oriented along 030^0 East. In station 8 with square length "a" = 50 metres shows maximum apparent resistivity along 090^0 East, which was perpendicular to 000^0 East, which was interpreted as the azimuth along which the fracture in the region cuts through. In station 9, using "a"=40 metres the azimuthal polar plot drawn showed fracture strike along 060^0 East (NE-SW) direction. In survey station 10 using "a"=40 metres the fracture strike was denoted along 030^0 Azimuth. Survey station 11 and 12 both had a square length of "a"=40 metres, and different fracture orientations. In station 11 fracture present cut along 030^0 East, while station 12 the fracture was suspected along 090^0 East. The survey stations showed presence of fracture strike along different various orientations. One station showed fracture strike along N-S orientation, eight stations along NE-SW direction and three stations along NW-SE. According to the anomaly contour maps generated from both the resistivity and the porosity data, the main fracture strike was denoted along the NE-SW direction. The crossed square approach also displayed presence of a fracture along 039.3164^0 an azimuth in NE-SW direction as well.

4.4 Gravity data analysis

4.4.1 Qualitative analysis

After gravity reduction, Surfer 10 software was used in generating a contour map (Figure 4.11) that showed areas of distinct gravity anomalies within the study area. This was done by uploading the complete bouguer anomaly data on a worksheet in Surfer 10

software. Complete bouguer anomaly map was created from gridded data and the original corrected data was not necessarily honored in the grid file.

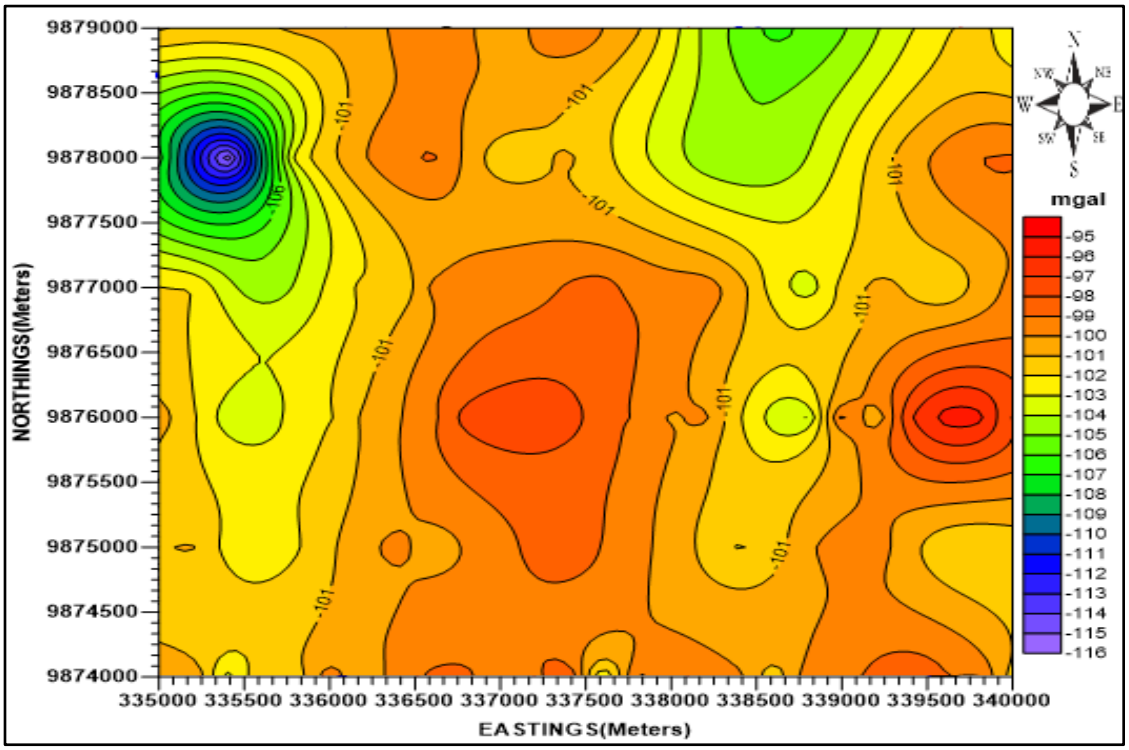

Figure 4.11: Complete bouguer anomaly contour map

This happened because the locations of the contour lines are determined solely by the interpolated grid node values and not directly by the original data. Interpolation is a method of constructing new data points within the range of discrete set of known data points. Kriging grid method was used to control the interpolation procedures. This method produced visually appealing map from irregularly spaced gravity data. This map shows three distinct zones. At the centre the map displays a zone dominated with substances of very high density. Towards the northeastern side, a region with substances of average density is observed .The western side shows presence of substance of low-density values, this correlates with the observation made using the geometric resistivity

data. According to Odero *et al.*, (2016) geo-electrical resistivity carried out on the same area of study showed a porous zone along the western side.

This western region was suspected to be dominated by a fractured rock, filled with a low-density material, which could possibly be either water, sediments or weathered materials. The qualitative description given was backed up by the geological report of the area, which showed that metamorphic rocks overlain by a plateau cover the entire region. Igneous rocks, the meta-intrusive mafic and ultramafic rocks that include diorites, Gabbros anorthosites, periodotites and picrites, describe the study area. Their low silica and gas contents make them very fluid (Nyamai *et al.*, 2003). Such a geological system may hold water in a network of fractures and faults since metamorphic rocks are non-porous and impervious. Therefore, the zone of interest in this study is the western side of the survey area. The visual inspection of complete bouguer anomaly map (Figure 4.11) showed a linear trend elongated in North-South directions along the western parts of the studied area. In general, the complete bouguer anomaly map showed low gravity gradient zones in the western parts relative to the Eastern parts. An insight that can be drawn from this map is that, along the western region, the rock beneath could be fractured. In addition, when a geo-electrical resistivity method was brought into consideration, a consistency was observed. To estimate gravity anomaly depicted, a cross-section AA' as shown in figure 4.12 .The data in table 4.9 was considered then uploaded in a 2D Euler deconvolution software.

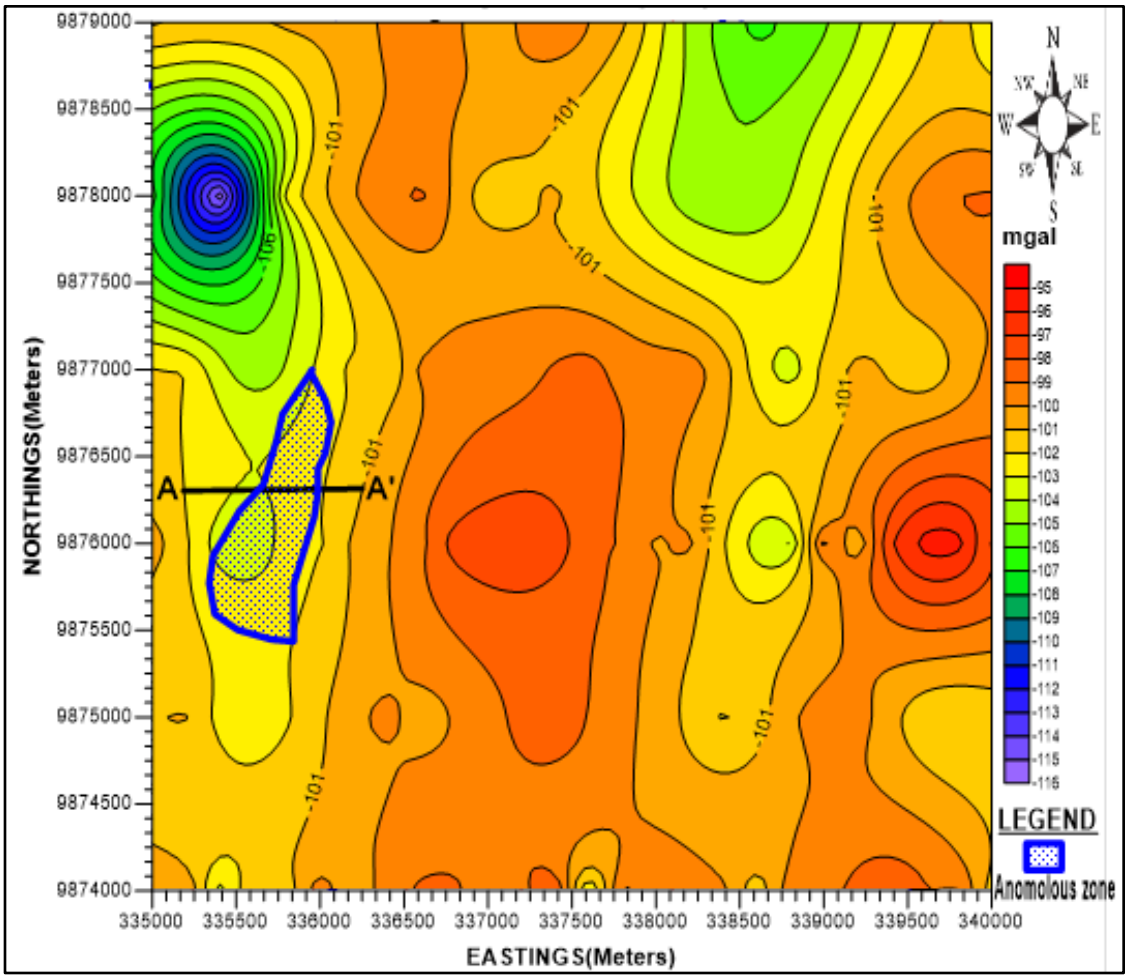

Figure 4.12: Cross-section AA' on Complete Bouguer anomaly contour map

4.4.2 2D Euler Deconvolution Curve

Using data in Table 4.9, a 2D Euler deconvolution curve covering a kilometer distance (AA') was generated and discontinuity covering a distance of 600 meters was observed (Figure 4.13).

Table 4.9: Cross-section AA' data

Distance in Meters	Complete Bouguer anomaly
0	-4.382E-06
16.64958881	-0.085295842
67.15775681	-0.346720568
117.6659248	-0.600325165
168.1740928	-0.835390834
218.6822608	-1.042101511
269.1904288	-1.212803198
319.6985968	-1.342693921
370.2067648	-1.429831806
420.7149328	-1.474875165
471.2231008	-1.480825816
521.7312689	-1.452535471
572.2394369	-1.395718505
622.7476049	-1.315690692
673.2557729	-1.216384035
723.7639409	-1.100097718
774.2721089	-0.968049783
824.7802769	-0.821359422
875.2884449	-0.661885973
925.7966129	-0.492467515
976.3047809	-0.316475403
1026.812949	-0.137000836
1065.074018	1.68988E-06

Constraint parameters applied were the Structural indices of 1.5 and 100 meters depth. The 2D Euler deconvolution curve generated showed discontinuity along the region where a substance of low density beneath the subsurface was suspected.

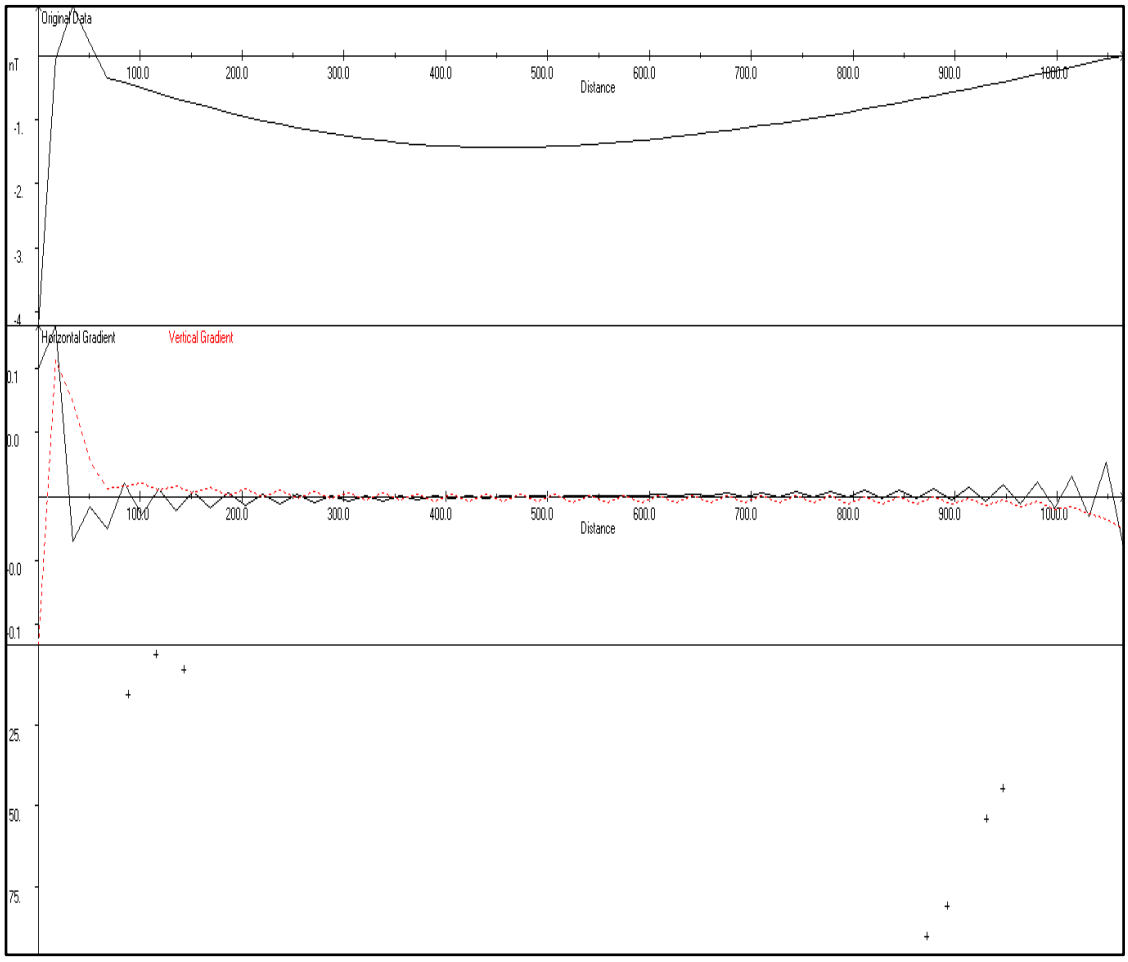

Figure 4.13: 2D Euler deconvolution Curve

In an attempt to understand the causative of the anomaly depicted, the same cross-section (AA') data was uploaded in Grav2dc software and a forward model was created (Figure 4.14).

4.4.2 Grav2dc forward model

Along the same region where discontinuity was observed using 2D Euler deconvolution software a body of low density was detected. It was noted that the region along the western side showed presence of a low-density substance covered 600 meters distance penetrating up to a depth of 70 meters approximately.

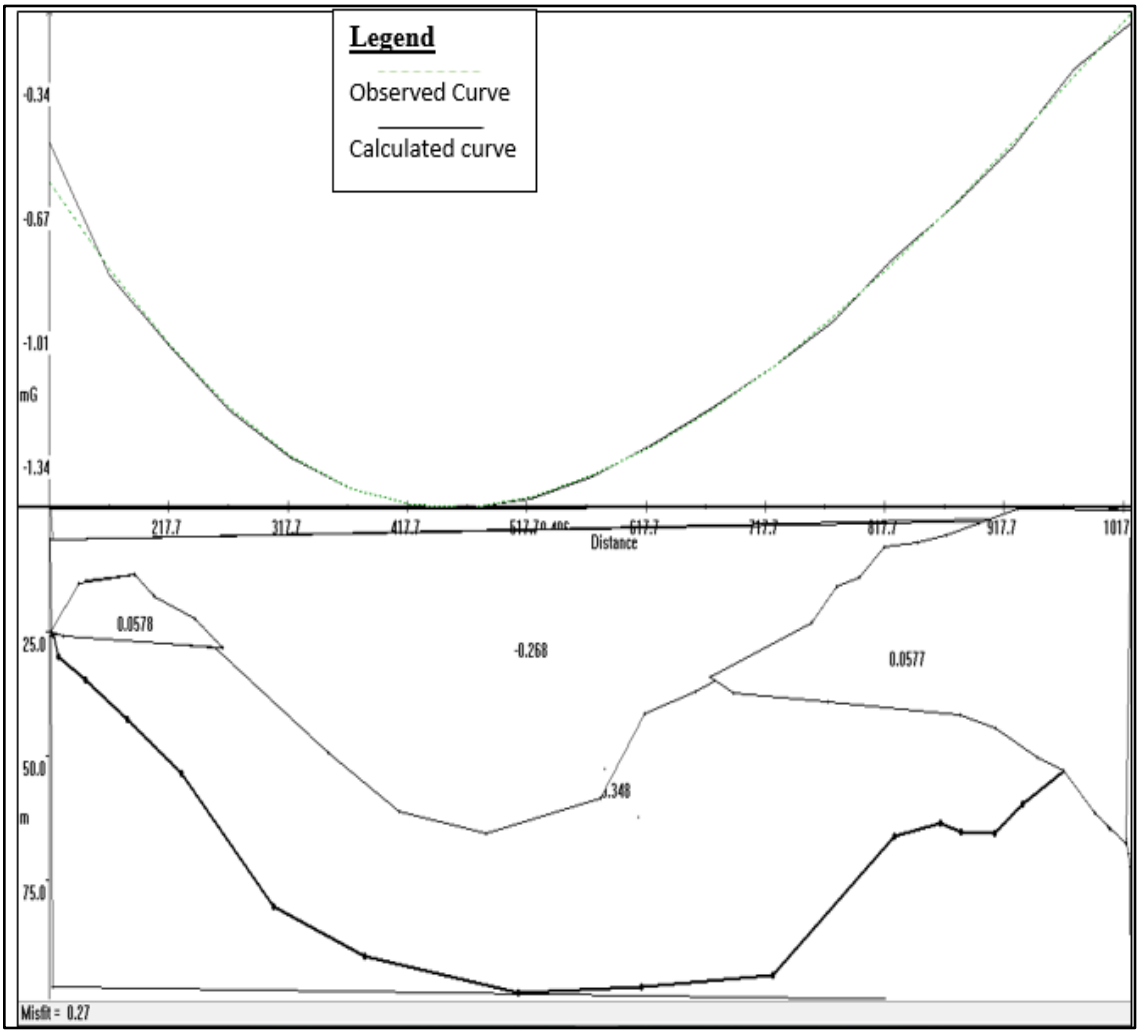

Figure 4:14: Grav2dc forward model

4.5 Data correlation

Approaches deployed in data analysis produced results that showed a correlation. Geometric apparent resistivity data displayed the main fracture along the 60-240 azimuth within the study area. Azimuthal polar charts, porosity and crossed array data showed presence of a fracture along 039.13245^0 orientation. This region has a possibility of having several fractures with the main one being oriented along 049.56622^0 orientation. This value is determined by getting the average of the fracture strike azimuths displayed by the utilized techniques used in analyzing the azimuthal square array data. Gravity results showed presence of a low-density substance along the western side of the study area stretching from North East to southwest. This indicated the investigated fractured zone. Data analysis using Grav2dc confirmed that the area has four subsurface system with an overburden made of black top soil, weathered Micaceous, Biotite and a hard gneiss basement rock. Within the weathered Micaceous layer a characteristic of an aquiferous region was detected with a width of about 600 meters and a depth of about 70 meters.

Upon integration of the data from the two methods applied, an overall anomalous zone was produced (Figure 4.16) by overlaying the regions of interest displayed by the Geometric resistivity, porosity and complete Bouguer anomaly contour maps (Figure 4.15).

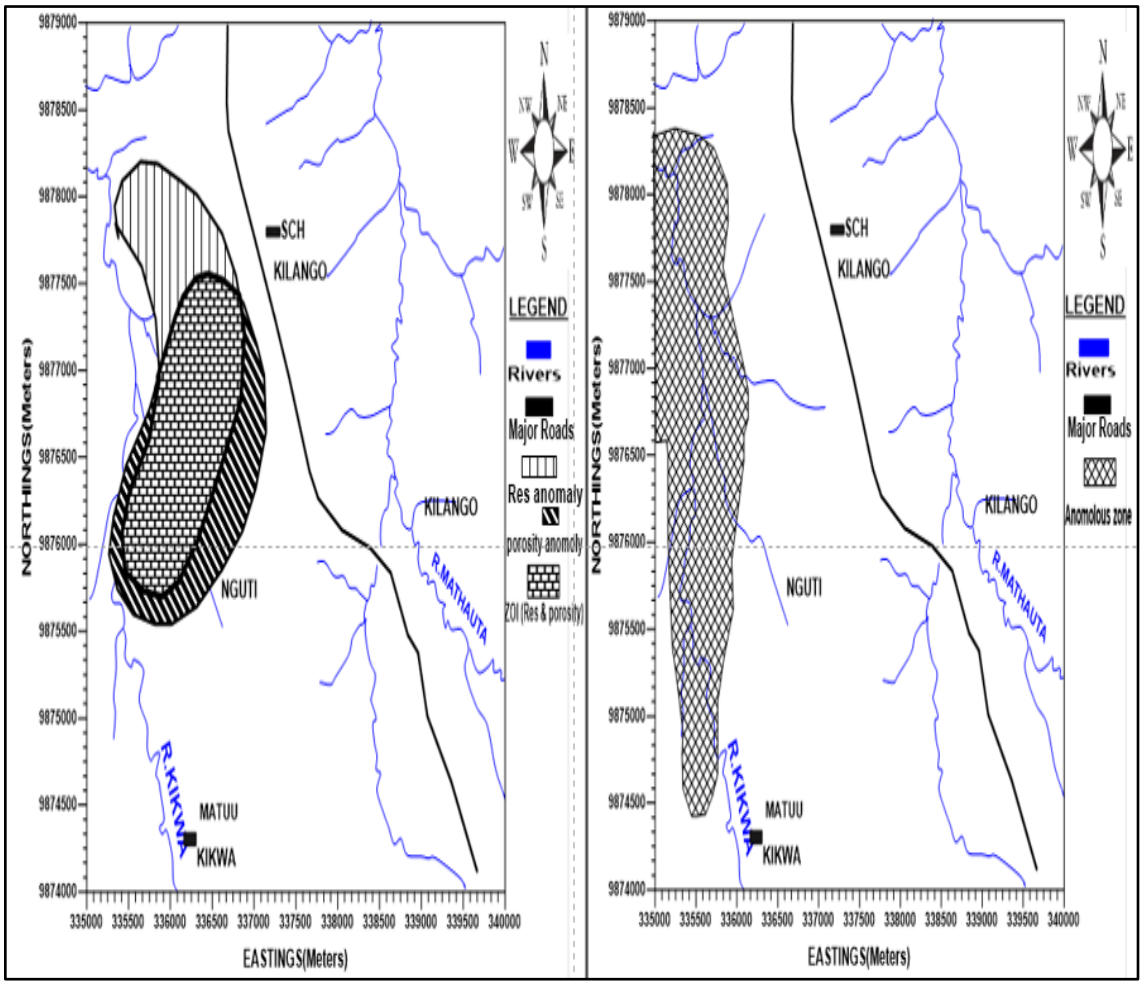

Figure 4.15: Delineated anomalous zones

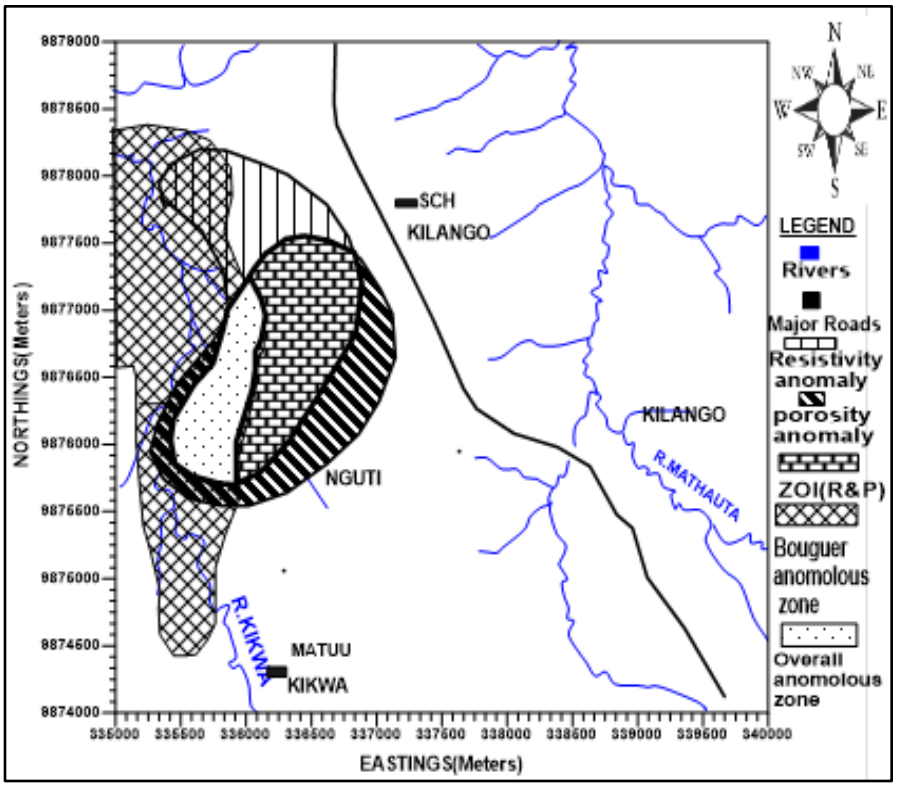

Figure 4.16: Integration of Primers over the study area

4.6 Aquifer Geometry

An aquiferous zone was detected at the western side of study area, on the third layer which is made of Loose/weathered micaceous gneisses with thickness ranging from 10m to about 55m towards the North and a lateral stretch width 600m and a depth of 70m approximately. Best ground water yields can be harnesses at the delineated overall anomalous zone. This information was utilised in coming up with a schematic diagram of the Geo-hydrological model observed in the study area as shown in figure 4.17.

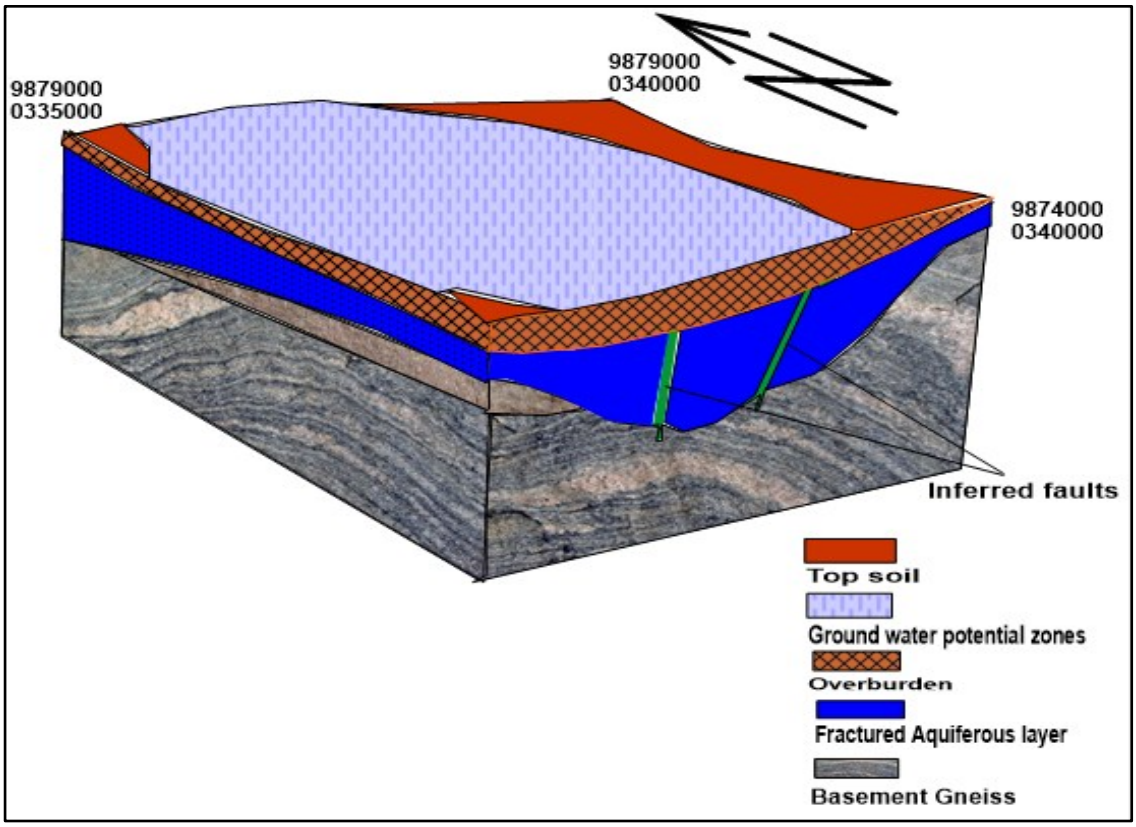

Figure 4.17: Geo-hydrological model for the area (Not to scale)

In order to validate the results obtained from this research, a proper analysis of various research articles was conducted. It was established that, most of the researchers who have conducted ground water exploration using Geo-electrical resistivity and gravity methods have obtained values that lie within the range of the values detected in this work. The apparent resistivity values of interest in this research were ranging from 50 up to 90 Ωm. According to Parkhomenko, 2012, natural water in igneous rocks has apparent resistivity ranging from 0.5 to 150 Ωm. Borehole logging research conducted in Masvingo Province in Zimbabwe indicated that groundwater is usually fresh with apparent resistivity that range from 10 to 100 Ωm (Shedlock 1987). Porosity values obtained from this research ranged from 24% to 29%, Porosity exceeding 20% is large and weathered metamorphic rocks have 20-30% (Fetter, 2018). Residual gravity

anomaly changes detected in the study area had a range of -0.3165 up to -1.4808. According to the research titled “The gravity method in groundwater exploration in crystalline rocks: a study in the peninsular granitic region of Hyderabad, India” by Murty and Raghavan, 2002 indicated that Weathered Gneiss gives residual gravity anomaly ranging from -0.1 to -0.7.

CHAPTER FIVE

CONCLUSIONS AND RECOMMENDATIONS

5.1 Conclusion

Integrated inferences from the electrical resistivity and gravity anomaly trends, 2D Euler deconvolution curve, forward- modeling, porosity analysis and crossed square array data conducted over the study area revealed that the western side is a groundwater potential zone. This was based on the findings of the delineated primers and the inferred aquifer. Along the western side of the study area, a low resistive and a less porous zone was detected. In addition, gravity results showed presence of a substance of low density along the same region It was suspected that, around this region there could be fractures in the bedrock that are probably filled with ground water or sediments. Boreholes sited at the western side of the study area have a high possibility of registering relatively greater percentage of success especially along the overall anomalous zone compared to the rest of the regions within the study area. In summary, Kilango-Matuu area has a high possibility of having a fractured basement rock, which is capable of holding and transmitting ground water.

5.2 Recommendation

In this research, it was possible to identify the suspected aquifer within the study area. However, there is need to drill a borehole at the center of the delineated overall anomalous zone. In addition, further research need to be conducted past the western boundary of the study area to investigate whether the region has a fractured bedrock as well.

REFERENCES

Antony A. (2012). Azimuthal Square array configuration and Groundwater prospecting in Quartzite Terrain at Edaikkal, Ambasamudram, Tirunelveli, *Research Journal of earth sciences, 4*(2), 49-55.

Archie, G. E. (1942). The electrical resistivity log as an aid in determining some reservoir characteristics. *Transactions of the AIME*, *146* (01), 54-62.

Baker, B.H. (1954). Geology of the Southern Machakos area*, Geological Survey report Kenya*, (27), 13.

Batte, A. G., Muwanga, A., Sigrist, P. W., and Owor, M. (2008). Vertical electrical sounding as an exploration technique to improve on the certainty of groundwater yield in the fractured crystalline basement aquifers of eastern Uganda. *Hydrogeology journal*, *16*(8), 1683-1693.

Bear, L.M. (1952). The Geology of the area Southeast of Embu. *Geological survey report Kenya,* (23)**,** 45.

Bills D., Truini M., Flynn M., Pierce H., Catchings R. and Rymer M. (2000). Hydrogeology of the regional aquifer near Flagstaff, Arizona. U.S Geological Survey report: Water resources investigations 100-4122.

Bisson, R. A., and Lehr, J. H. (2007). Discovering new water resources in consolidated rocks using innovative hydro-geologic concepts, exploration, drilling, aquifer testing and management methods. *Modern groundwater exploration*, 79-112.

Busby, J. P. (2000). The effectiveness of azimuthal apparent-resistivity measurements as a method for determining fracture strike orientations. *Geophysical prospecting*, *48*(4), 677-695.

Chandler V. (1994). Gravity investigation for potential ground-water resources in rock county, Minnesota. University of Minnesota: Report of investigation 44.

Cooper G.R.J. (2004). Euler deconvolution applied to potential field gradients, *Exploration Geophysics*, (35**)**, 165-170.

Cooper, G. R. J. (2006). Interpreting potential field data using continuous wavelet transforms of their horizontal derivatives. *Computers & Geosciences*, *32*(7), 984-992.

Crowther, A. F. (1957). *Geology of the Mwingi area, North Kitui: degree sheet 45, south-west quarter* (No. 38). Geological Survey of Kenya.

Dobrin, M. B., and Savit, C. H. (1960). *Introduction to geophysical prospecting* (Vol. 4). New York: McGraw-hill.

Dodson R.G. (1953). Geology of the North Kitui area, *Geological survey report Kenya***,** (33), 68.

Dodson R.G. (1963). Geology of the south Horr area, *Geological survey report Kenya* (60), 50.

Dodson R.G. (1991). Geology of the Barchuma-Kom area, *Geological survey report Kenya*, (93), 73.

Fairburn, W.A. (1958). Geology of the Fort Hall area, *Geological survey report Kenya, 73*, 47.

Fetter, C. W. (2018). *Applied hydrogeology*. Illinois: Waveland Press.

Foster, S., Chilton, J., Moench, M., Cardy, F., and Schiffler, M. (2000). Groundwater in rural development. *World Bank technical paper*, *463*.

Goldman, M., Rabinovich, B., Rabinovich, M., Gilad, D., Gev, I., and Schirov, M. (1994). Application of the integrated NMR-TDEM method in groundwater exploration in Israel. *Journal of Applied Geophysics*, *31*(1-4), 27-52.

Habberjam, G. (1975). Apparent resistivity, anisotropy and strike measurements. *Geophysical prospecting*, *23*(2), 211-247.

Habberjam G. and Watkins G. (1967). The use of a square configuration in resistivity prospecting. *Geophysical prospecting, 15*(3), 445-467**.**

Hammer, S. (1939). Terrain corrections for gravimeter stations. *Geophysics*, *4*(3), 184-194.

K'Orowe M., Nyadawa M., Singh V. and Rangarajan R. (2012). Geo-electric resistivity and groundwater flow models for characterization of hard rock aquifer system, *Global Advanced Research Journal of Physical and Applied Science*, *1*(1), 12-13.

Keary P., Brooks M. and Hill I. (2002). *An Introduction to Geophysical Exploration*. London: Blackwell Scientific Publications**.**

Keating, P. B. (1998). Weighted Euler deconvolution of gravity data. *Geophysics*, *63*(5), 1595-1603.

Lane J., Haeni F. and Watson W. (1995). Use of square-array direct current resistivity methods to detect fractures in crystalline bedrock in New Hampshire. *Groundwater, 23*(2), 211-247.

Lashkaripour, G. R. (2003). An investigation of groundwater condition by geoelectrical resistivity method: A case study in Korin aquifer, southeast Iran. *Journal of Spatial Hydrology*, *3*(2).

Lattman, L. H. (1958). Technique of mapping geologic fracture traces and lineaments on aerial photographs. *Photogrammetric Engineering*, *24*(4), 568-576.

Mark T. (1980). A gravity survey of a deep buried valley. *Groundwater*, *18* (1),24-29.

Mason P. (1955). Geology of the Meru-Isiolo area *Geological survey report, Kenya*, (31),44.

Mathu E. (1992). The Mutito faults in the Pan-African Mozambique Belt, Eastern Kenya. In Mason R. (Ed.), Basement Tectonics. 61-69. Kluwer Academics Publishers, Netherlands.

Matias, M. S., and Habberjam, G. M. (1986). The effect of structure and anisotropy on resistivity measurements. *Geophysics, 51*(4), 964-971.

Mishra, D. C. (2011). Gravity and magnetic methods for geological studies. Hyderabad: BS Publications.

Murty B. and Raghavan V. (2002). The gravity method in groundwater exploration in crystalline rocks: A study in the peninsular granitic region of Hyderabad, India. *Hydrogeology Journal,* (10), 307–321.

Mushayandebvu, M. F., Lesur, V., Reid, A. B., and Fairhead, J. D. (2004). Grid Euler deconvolution with constraints for 2D structures. *Geophysics*, *69*(2), 489-496.

Muturi E., K'orowe M., Githiri G., Cezar I. and. Jeffrey S. (2013). Application of Geophysics for groundwater evaluation in hard rock: Case study: Kitui fault zone. Paper presented at JKUAT Scientific Technological and Industrialization Conference, held at AICAD center, Nairobi, Kenya. November 14th-15th, 2013.

Ndeto R. (2011). Water projects in Yatta District. Projects brief reports WD/YAT/1/4/21. Tanathi Water Services Board, Kithimani, Kenya.

Nyamai C., Mathu E., Opiyo N. and Wallbrecher E. (2003). A Reappraisal of the Geology, geochemistry, structures and tectonics of the Mozambique belt in Kenya, East of the Rift

system .*African Journal of Science and Technology Science and Engineering Series*, *4* (2), 51-71.

Odero E, O., K'Orowe M, O., and Githiri J, G. (2016). Integrated Resistivity Techniques for Groundwater Potential Evaluation in Matuu, Machakos County, Kenya.

Omoyo, N. N., Wakhungu, J., and Oteng'i, S. (2015). Effects of climate variability on maize yield in the arid and semi-arid lands of lower eastern Kenya. *Agriculture & Food Security*, *4*(1), 8.

Overmeeren, R. V. (1975). A combination of gravity and seismic refraction measurements, applied to groundwater explorations near Taltal, Province of Antofagasta, Chile. *Geophysical Prospecting*, *23*(2), 248-258.

Parkhomenko, E. I. (2012). *Electrical properties of rocks*. Berlin: Springer Science & Business Media.

Reynolds J. (1998). An Introduction to Applied and Environmental Geophysics. New York: John Wiley & Sons.

Sanders, L.D. (1965). Geology of the contact between the Nyanza Shield and the Mozambique belt in western Kenya. *Geological survey report Kenya* (7).

Shedlock, S. L. (1987). Borehole logging in Masvingo Province, Zimbabwe. *Unpublished report of British Geological Survey, WD/OS/87/7*.

Singhal, B. B. S and Gupta, R. P. (2010). Applied hydrogeology of fractured rocks. Springer Science & Business Media.

Sivaramakrishnan, J., Asokan, A., Sooryanarayana, K. R., Hegde, S. S., and Benjamin, J. (2015). Occurrence of Ground Water in Hard rock under distinct Geological setup. *Aquatic Procedia*, (4), 706-712.

Smith, K. C. A., and Alley, R. E. (1992). Electrical circuits: An introduction. England: Cambridge University Press.

Sri N. and Oliver A. (2003). Aquifer parameter estimation from surface resistivity data. *Ground water, 41* (1):94-9

Sultan, S. A., Mekhemer, H. M., Santos, F. A. M., and Alla, M. A. (2009). Geophysical measurements for subsurface mapping and groundwater exploration at the central part of the Sinai Peninsula, Egypt. *Arabian journal for science and engineering*, *34*(1), 103.

Survey of Kenya, (2005). Topographical map of Matuu area. Report Survey of Kenya 150/1. The government Printer, Nairobi.

Taylor, R. W., and Fleming, A. H. (1988). Characterizing jointed systems by azimuthal resistivity surveys. *Groundwater*, *26*(4), 464-474.

Trochu, F. (1993). A contouring program based on dual kriging interpolation. *Engineering with computers*, *9*(3), 160-177.

Watson, K. A., and Barker, R. D. (1999). Differentiating anisotropy and lateral effects using azimuthal resistivity offset Wenner soundings. *Geophysics*, *64*(3), 739-745.

Yutsis V., Yaneth Q., Konstantin K., Juan C. and Gabriel C. (2012). Gravity Field Variations Associated with the Buried Geological Structures: San Marcos Fault (NE Mexico) Case Study. .*Journal of Modern Physics*, (3):1236-1246.

APPENDICES

Appendix I: Raw Resistivity Data

STATION 1

$\rho_{a\alpha}$	$\rho_{a\beta}$	$\rho_{a\alpha} * \rho_{a\beta}$	SQR($\rho_{a\alpha} * \rho_{a\beta}$)	AZIMUTH	RES-GEOMERIC MEAN
112.7649	92.91911	10478.01579	102.3621795	0	102.3621795
213.2404	98.05113	20908.46705	144.5976039	30	144.5976039
112.5954	193.5363	21791.29554	147.6187506	60	147.6187506
92.35485	227.3063	20992.83851	144.8890559	90	144.8890559
99.50148	216.8084	21572.75752	146.8766745	120	146.8766745
192.9012	110.9842	21408.97522	146.3180619	150	146.3180619
100.4305	91.85066	9224.60572	96.044811	180	96.044811
213.5773	112.9151	24116.10097	155.293596	210	155.293596
112.87	193.8817	21883.43308	147.9305009	240	147.9305009
93.83953	225.8946	21197.83929	145.5947777	270	145.5947777
114.4556	197.0892	22557.95351	150.1930541	300	150.1930541
202.3692	107.103	21674.34495	147.222094	330	147.222094

STATION 2

$\rho_{a\alpha}$	$\rho_{a\beta}$	$\rho_{a\alpha}{}^{*}\rho_{a\beta}$	SQR($\rho_{a\alpha}{}^{*}\rho_{a\beta}$)	Azimuth	Geometric resistivity
158.7793	111.8574	17760.63	133.2690246	0	133.2690246
197.5569	94.39307	18648	136.5576868	30	136.5576868
145.4558	110.9606	16139.85	127.0427236	60	127.0427236
109.772	157.8782	17330.6	131.6457196	90	131.6457196
201.2386	99.11315	19945.39	141.2281418	120	141.2281418
111.9217	145.533	16288.31	127.6256536	150	127.6256536
158.7793	109.6518	17410.43	131.9486066	180	131.9486066
198.9858	97.50403	19401.92	139.2907657	210	139.2907657
148.1763	109.6346	16245.25	127.4568595	240	127.4568595
117.5343	157.7666	18542.99	136.1726649	270	136.1726649
93.40185	196.6987	18372.02	135.5434352	300	135.5434352
110.8275	146.2839	16212.29	127.3274831	330	127.3274831

STATION 3

$\rho_{a\alpha}$	$\rho_{a\beta}$		Azimuth	Geometric Resistivity
299.2103	192.5665	57617.87969	0	240.0372465
398.7483	150.4805	60003.84621	30	244.9568252
362.8756	181.9506	66025.43916	60	256.9541577
189.9662	301.0941	57197.67946	90	239.1603635
144.4817	401.649	58030.9357	120	240.8961098
132.5571	427.1074	56616.10662	150	237.9413933
300.2745	192.5965	57831.82133	180	240.4824761
396.813	148.5024	58927.67805	210	242.750238
364.6178	182.4612	66528.6062	240	257.9313982
191.9829	301.5232	57887.29422	270	240.5977852
148.9744	396.753	59106.02761	300	243.1173125
139.3797	427.1846	59540.8824	330	244.0100047

STATION 4

$\rho_{a\alpha}$	$\rho_{a\beta}$	$\rho_{a\alpha}{}^{*}\rho_{a\beta}$	SQR($\rho_{a\alpha}{}^{*}\rho_{a\beta}$)	Azimuth	Geometric Resistivity
161.5512	101.9194	16465.213	128.3168442	0	128.3168442
180.9379	103.4299	18714.384	136.8005258	30	136.8005258
192.309	100.2717	19283.153	138.8637913	60	138.8637913
100.9454	162.4953	16403.147	128.0747715	90	128.0747715
105.5367	177.9213	18777.239	137.0300659	120	137.0300659
101.3487	193.0042	19560.728	139.8596722	150	139.8596722
161.5212	98.95866	15983.923	126.427539	180	126.427539
175.4969	105.85	18576.348	136.2950771	210	136.2950771
192.7681	100.9154	19453.266	139.4749638	240	139.4749638
102.872	161.3925	16602.773	128.8517494	270	128.8517494
106.5022	174.9177	18629.117	136.4885249	300	136.4885249
100.2245	183.7485	18416.102	135.7059405	330	135.7059405

STATION 5

$\rho_{a\alpha}$	$\rho_{a\beta}$			Azimuth	Geometric Resistivity
141.8213	126.1549	17891.45	133.7589	0	133.7589412
212.6418	71.78279	15264.02	123.5477	30	123.5476622
209.6392	81.27337	17038.09	130.53	60	130.5300238
127.8123	140.8365	18000.64	134.1665	90	134.1664668
71.98554	213.9935	15404.44	124.1146	120	124.1146152
82.62503	207.512	17145.68	130.9415	150	130.9415271
139.7809	128.9709	18027.67	134.2672	180	134.2671584
213.4432	72.30736	15433.51	124.2317	210	124.2316941
209.3592	82.46734	17265.3	131.3975	240	131.3974867
127.5227	141.3482	18025.1	134.2576	270	134.2575959
72.69355	213.0763	15489.27	124.4559	300	124.4559093
81.14143	208.5289	16920.34	130.0782	330	130.0781881

STATION 6

$\rho_{a\alpha}$	$\rho_{a\beta}$			Azimuth	Geometric mean resistivity
71.21746	60.21967	4288.692	65.48811	0	65.4881057
79.84663	51.76643	4133.375	64.29133	30	64.2913297
84.68257	55.9201	4735.458	68.81466	60	68.81466439
61.17656	73.64187	4505.156	67.12046	90	67.12045916
52.98078	79.28022	4200.328	64.80994	120	64.80993651
54.43542	85.16316	4635.893	68.08739	150	68.08738951
71.08873	60.45567	4297.717	65.55698	180	65.55697653
79.99252	52.92071	4233.261	65.06351	210	65.06351362
86.09859	53.7789	4630.288	68.04622	240	68.04621876
61.34391	70.65105	4334.012	65.83321	270	65.83321012
53.12238	78.80392	4186.252	64.70125	300	64.70125189
54.5427	84.41224	4604.071	67.85331	330	67.85330598

STATION 7

$\rho_{a\alpha}$	$\rho_{a\beta}$			Azimuth	Geometric mean Resistivity
121.3069	210.2618	25506.22	159.7067	0	159.7067
119.1072	211.2651	25163.2	158.6291	30	158.6291
70.84733	222.2208	15743.75	125.4741	60	125.4741071
103.3872	215.3158	22260.9	149.2009	90	149.2008734
111.7623	210.5462	23531.12	153.3986	120	153.3985541
113.6776	211.7801	24074.67	155.1601	150	155.1601375
86.27226	203.7055	17574.14	132.5675	180	132.5674764
99.59939	207.091	20626.13	143.618	210	143.6180127
90.18884	144.8494	13063.8	114.297	240	114.2969811
127.6808	204.2045	26072.99	161.4713	270	161.4713342
94.37369	211.2007	19931.79	141.18	300	141.1799924
107.7437	209.9506	22620.87	150.4023	330	150.4023459

STATION8

$\rho_{a\alpha}$	$\rho_{a\beta}$			Azimuth	Geometric mean Resistivity
103.5018	75.21344	7784.723	88.23108	0	88.23107655
120.3589	65.49758	7883.216	88.78747	30	88.787474
116.777	63.06137	7364.117	85.81443	60	85.81443364
101.2844	76.80969	7779.622	88.20217	90	88.2021652
66.5596	119.4706	7951.918	89.17353	120	89.17352985
109.8449	69.0473	7584.493	87.089	150	87.08899653
102.6779	76.12098	7815.941	88.40781	180	88.40781333
120.8931	65.72607	7945.83	89.13938	210	89.13938303
118.9879	62.78782	7470.992	86.4349	240	86.43490095
102.8388	76.23684	7840.105	88.54437	270	88.54436617
66.16054	120.3814	7964.499	89.24404	300	89.24404041
109.8867	68.77696	7557.676	86.9349	330	86.93489606

STATION 9

$\rho_{a\alpha}$	$\rho_{a\beta}$			Azimuth	Geometric mean Resisitivity
74.16108	163.2162	12104.29	110.0195	0	110.0194801
75.50845	163.5423	12348.82	111.1253	30	111.1252573
23.96515	27.68972	663.5882	25.76021	60	44.65484509
162.255	73.75558	11967.21	109.3947	90	109.3947429
163.1282	74.94633	12225.86	110.5706	120	110.5706057
114.3011	111.0056	12688.06	112.6413	150	112.6412974
73.24924	164.01	12013.61	109.6066	180	109.6066035
74.8176	165.1106	12353.18	111.1449	210	111.1448623
25.91111	31.72968	822.1512	28.67318	240	28.67317842
164.5099	75.04073	12344.94	111.1078	270	111.1077943
164.3383	75.04502	12332.77	111.053	300	111.0529927
116.1162	109.0253	12659.6	112.5149	330	112.5149014

STATION 10

$\rho_{a\alpha}$	$\rho_{a\beta}$			Azimuth	Geometric mean Resistivity
190.0992	198.0847	37655.73	194.0508	0	194.0508431
189.7859	202.4014	38412.94	195.9922	30	195.9921829
177.3249	242.9469	43080.54	207.5585	60	207.5585119
198.7283	189.271	37613.51	193.942	90	193.9420216
203.7659	188.9663	38504.9	196.2267	120	196.2266618
212.7212	248.8556	52936.87	230.0801	150	230.0801293
155.8914	198.2949	30912.48	175.8195	180	175.8194578
188.1553	203.1566	38225	195.5122	210	195.5121549
177.4837	212.4681	37709.61	194.1896	240	194.1896201
198.4666	206.1989	40923.59	202.2958	270	202.2958091
202.7661	188.6831	38258.55	195.5979	300	195.5979295
213.0259	177.621	37837.86	194.5196	330	194.5195743

STATION 11

$\rho_{a\alpha}$	$\rho_{a\beta}$			Azimuth	Geometric mean resisitivity
171.7767	173.1884	29749.72	172.4811	0	173.67805
157.3117	192.9827	30358.45	174.2368	30	173.67215
165.7993	181.3155	30061.99	173.3839	60	173.3839318
175.0807	171.5921	30042.47	173.3277	90	173.3276516
193.5791	156.1703	30231.32	173.8716	120	173.8715683
180.8135	164.8124	29800.3	172.6276	150	173.7436
172.7979	174.4371	30142.36	173.6156	180	173.6155532
156.8011	192.2361	30142.83	173.6169	210	173.6169085
165.4389	180.865	29922.09	172.98	240	173.50395
174.0509	172.7335	30064.42	173.391	270	173.39096
192.6308	156.947	30232.83	173.8759	300	173.8759183
182.444	165.3445	30166.11	173.6839	330	173.6839471

STATION 12

$\rho_{a\alpha}$	$\rho_{a\beta}$			Azimuth	Geometric mean resisitivity
130.9909	261.3166	34230.09	185.0137	0	185.0137472
274.2325	236.3259	64808.24	254.5746	30	178.0897
274.3698	62.51963	17153.5	130.9714	60	171.165675
260.7459	130.3215	33980.79	184.3388	90	184.3387872
153.2997	195.4586	29963.74	173.1004	120	173.1003755
102.5674	312.6711	32069.86	179.0806	150	179.0805855
130.33	261.72	34109.97	184.6889	180	184.6888588
192.073	155.1663	29803.25	172.6362	210	172.636178
313.9713	102.6189	32219.38	179.4976	240	179.4975707
263.0416	130.536	34336.4	185.3008	270	185.3008356
153.4756	194.3	29820.32	172.6856	300	172.6855974
102.5588	301.639	30935.73	175.8856	330	175.8855649

Appendix II: Geometric Resistivity Data

STATIONS	EASTINGS	NORTHINGS	GEOMETRIC	ELEVATION

			RESISTIVITY VALUE	
STN1	335515	9878124	99.20349525	1206
STN2	337787	9878242	137.9242263	1198
STN3	339249	9878351	240.9757	1204
STN4	338225	9876102	139.1693776	1217
STN5	339691	9877525	134.01305	1204
STN6	335895	9876291	67.97034775	1206
STN7	336425	9877486	88.96342852	1215
STN8	337587	9874717	119.8855441	1229
STN9	335301	9874396	36.664015	1221
STN10	336710	9875323	200.874066	1218
STN11	335615	9875204	173.6445293	1214
STN12	335132	9877212	175.3316229	1202

Appendix III: Water Conductivity Data

Northings	Eastings	WATER CONDUCTIVITY($\mu S/cm$)

9876351	335877	281
9877490	334758	136
9874063	334077	163
9874000	335800	111
9875000	339600	221

Appendix IV: Gravity Data

EASTINGS	NORTHINGS	COMPLETE BOUGUER ANOMALY(mgal)

335000	9879000	-103.671365
335400	9879000	-101.4190754
335800	9879000	-101.1278016
336200	9879000	-100.7824928
336600	9879000	-99.38802763
337000	9879000	-100.7396757
337400	9879000	-99.33259143
337800	9879000	-100.9725594
338200	9879000	-104.4007764
338600	9879000	-106.4617962
339000	9879000	-105.4779708
339400	9879000	-103.1933911
339800	9879000	-101.5424779
340200	9879000	-105.2443388
335000	9878000	-106.9677899
335400	9878000	-118.8962578
335800	9878000	-102.8438183
336200	9878000	-101.5368026
336600	9878000	-99.37146553
337000	9878000	-101.829396
337400	9878000	-101.0055642
337800	9878000	-102.8909641
338200	9878000	-104.8440889
338600	9878000	-105.1699428
339000	9878000	-103.012475
339400	9878000	-101.4534541
339800	9878000	-100.3156139
340000	9878000	-99.12051033

335000	9877000	-102.2775762
335200	9877000	-102.31411
335400	9877000	-103.913195
335600	9877000	-104.9775583
335800	9877000	-104.1617817
336000	9877000	-103.0181384
336200	9877000	-101.9052291
336400	9877000	-102.1926191
336600	9877000	-99.95227533
336800	9877000	-99.89932343
337000	9877000	-100.0108854
337200	9877000	-99.68666593
337400	9877000	-98.99277123
337600	9877000	-98.71684433
337800	9877000	-99.54271473
338000	9877000	-99.73936163
338200	9877000	-99.61050163
338400	9877000	-100.666508
338600	9877000	-102.4862489
338800	9877000	-103.5589691
339000	9877000	-101.8837822
339200	9877000	-100.9070558
339400	9877000	-101.1754994
339600	9877000	-101.8478263
339800	9877000	-100.74
340000	9877000	-99.77141453
335000	9876000	-101.0411693
335200	9876000	-102.2987776

335400	9876000	-103.7505166
335600	9876000	-103.8942116
335800	9876000	-102.7388221
336000	9876000	-102.2777114
336200	9876000	-101.0053562
336400	9876000	-100.2881386
336600	9876000	-99.48249411
336800	9876000	-97.80030891
337000	9876000	-97.88264891
337200	9876000	-98.05607391
337400	9876000	-97.84388891
337600	9876000	-99.19505081
337800	9876000	-99.28677771
338000	9876000	-100.3774691
338200	9876000	-101.6313998
338400	9876000	-103.8242457
338600	9876000	-103.4426364
338800	9876000	-104.1285709
339000	9876000	-104.6761243
339200	9876000	-101.5328696
339400	9876000	-103.1135572
339600	9876000	-102.3814258
339800	9876000	-101.7483713
340000	9876000	-98.27988561
340000	9875000	-101.5873042
339800	9875000	-102.0555969
339600	9875000	-101.7527999
339400	9875000	-100.7900035

339200	9875000	-99.56321831
339000	9875000	-99.64249831
338800	9875000	-100.2223709
338600	9875000	-101.5632792
338400	9875000	-102.2370778
338200	9875000	-101.3346562
338000	9875000	-100.4115747
337800	9875000	-99.87206431
337600	9875000	-99.13315771
337400	9875000	-98.66859201
337200	9875000	-98.72616691
337000	9875000	-99.53257451
336800	9875000	-100.2318572
336600	9875000	-100.580878
336400	9875000	-99.77536951
336200	9875000	-100.3952072
336000	9875000	-101.3041167
335800	9875000	-102.2847759
335600	9875000	-102.7603056
335400	9875000	-102.4730659
335000	9875000	-101.1619748
335200	9875000	-101.0628748
335000	9874000	-101.4095732
335200	9874000	-100.4099206
335400	9874000	-103.5860148
335600	9874000	-101.1551821
335800	9874000	-101.6345597
336000	9874000	-99.53260373

336200	9874000	-101.1807649
336400	9874000	-99.40754093
336600	9874000	-100.7699136
336800	9874000	-99.14507913
337000	9874000	-99.47395793
337200	9874000	-99.70187483
337400	9874000	-98.36838843
337600	9874000	-103.3068148
337800	9874000	-100.2120955
338000	9874000	-99.67008633
338200	9874000	-99.81546323
338400	9874000	-99.91148213
338600	9874000	-101.8249992
338800	9874000	-100.8766569
339000	9874000	-99.30480253
339200	9874000	-99.01664263
339400	9874000	-98.42717613
339600	9874000	-99.11869693
339800	9874000	-99.03941693
340000	9874000	-101.5825147